This is a preprint, the final version is subject to change, of the American Mineralogist (MSA)
Cite as Authors (Year) Title. American Mineralogist, in press.
(DOI will not work until issue is live.) DOI: http://dx.doi.org/10.2138/am-2017-5895

REVISION 1

Magmatic graphite inclusions in Mn-Fe-rich fluorapatite of perphosphorus granites (the Belvís pluton, Variscan Iberian Belt)

Cecilia Pérez-Soba[1], Carlos Villaseca[1, 2] and Alfredo Fernández [3]

[1] Departamento de Petrología y Geoquímica, Facultad de Ciencias Geológicas, Universidad Complutense de Madrid, c/ José Antonio Novais 12, 28040 Madrid, Spain

[2] Instituto de Geociencias IGEO (UCM, CSIC), c/ José Antonio Novais 12, 28040 Madrid, Spain

[3] Centro Nacional de Microscopía. Universidad Complutense de Madrid, 28040 Madrid, Spain

Abstract

Three Mn-Fe-rich fluorapatite types have been found in the highly evolved peraluminous and perphosphorous granites of the Belvís pluton. One of these apatite types includes abundant graphite microinclusions, suggestive of a magmatic origin for the graphite. The Belvís pluton is a reversely zoned massif composed by four highly fractionated granite units, showing a varied accessory phosphate phases: U-rich monazite, U-rich xenotime, U-rich fluorapatite and late eosphorite-childrenite. The strong peraluminous character of the granites determines an earlier monazite and xenotime crystallization, so the three types of fluorapatite records late stages of phosphate crystallization. The earlier type 1 apatite is mostly euhedral, small and clear; type 2 apatite is dusty, large (< 2800 μm) and mostly anhedral, with strong interlobates interfaces with

the main granite minerals, more abundant in the less fractionated units and absent in the most evolved unit; type 3 is subeuhedral to anhedral, shows feathery aggregate texture, and only appears in the most evolved unit. Apatite composition was acquired by electron microprobe analyses, laser ablation inductively coupled plasma-mass spectrometry and electron energy loss spectroscopy. Type 1 and type 2 apatite display similar broad compositional ranges showing high MnO (up to 4.30 wt%) and FeO (up to 2.88 wt%) contents, without traces of carbon in apatite structure. Type 2 differs from type 1 by having slightly higher LREE and Sr contents. REE spectra also differ, with type 1 displaying both variable LREE slope and negative Eu anomaly, whereas type 2 shows constant LREE slope and higher negative Eu anomaly, although both display similar HREE slope. Type 3 apatite displays higher FeO contents (up to 5.09 wt%), positively correlated with higher Cl-Na-Li-Be-B-Zn contents and extremely low Y-REE contents when compared to the other apatite types. Cation substitution indicates that part of the Fe content is as Fe^{3+}. Graphite has been found exclusively as abundant microinclusions in type 2 apatite, parallel or randomly distributed, and heterogeneously grouped in clusters within the crystals. High resolution electronic images show that graphite occurs with unusual habits: filaments of stacked hexagonal flakes up to 15 μm length and up to 0.5 μm width. Textural and chemical features suggest a highly crystallized melt which favor compartmentalizing in compositional microdomains where the apatite types would have crystallized. The cocrystallization of type 2 apatite and graphite suggests a C-F-P-rich melt, sufficiently saturated to acquire an immiscible character with the highly evolved silicate melt in late-magmatic stages. As type 2 differs from type 1 apatite by higher LREE and Sr contents, we interpret that fluxing components were favorably concentrated in those residual less-depleted LREE-Sr fraction melts, once monazite and zircon (and xenotime) would have crystallized. Type 3 apatite records a change in the ultimate melt stage: an increase of the

oxygen fugacity coupled with high undercooling by volatile lost of highly fractionated residual Cl-richer melts. The presence of biogenic carbon in granite peraluminous melts derived from metasedimentary sources and its later crystallization as graphite filaments open a discussion on the carbon behavior during magma evolution, especially in highly polymerized melt framework.

Key words: Mn-Fe-rich fluorapatite, graphite, granite, melt immiscibility, carbon isotope, perphosphorous, peraluminous

Introduction

Apatite, $Ca_5(PO_4)_3(Cl,OH,F)$, is a common accessory mineral within almost all igneous rocks. It shows a large compositional spectrum due to its favorable lattice for substitutions at different physicochemical conditions. These two characteristics make apatite a valuable tool for constraining magma evolution and thus many studies have related the apatite chemistry to different magmatic environments (e.g., Zhang et al. 1985; Sha and Chappel 1999; Belousova et al. 2002; Piccoli and Candela 2002; Hoshino et al. 2007; Buda and Pál-Molnár 2012; Marks et al. 2012; Mao et al. 2016) This is especially suitable for felsic peraluminous magmas, in which the high apatite solubility delays its crystallization (e.g., Wolf and London 1994). In this sense, some studies (e.g., Miles et al. 2013) point out the apatite as a suitable accessory mineral to record the late-stage magmatic crystallization history. Other phosphates (e.g,. monazite, xenotime) would have crystallized early, impoverishing residual magma mainly in REE (Wolf and London 1995) but favoring that volatile, fluxing components (e.g., C, F, Li) and others elements (e.g., Mn, Fe) may enter in later apatite.

Graphite may occur in many rock types, although published accounts of graphite in granitoids or high-silica volcanic rocks are rare. In these rocks graphite has been found in tiny amounts in different textural forms: as a solid phase within fluid inclusions (Frezzotti et al. 1994; Jaszczak and Trinchillo 2013), as small-size crystals interstitial to the main rock-forming minerals (Duke and Rumble 1986; Zeck 1992; Kanaris-Sotiriou 1997; Seifert et al. 2010) or hosted in these (Broska et al. 1992; Seifert et al. 2010), and as graphite spherulites interstitial or hosted in rock-forming minerals (Göd, 1989; Doroshkevich et al. 2007). Different origins have been invoked for graphite in igneous rocks: i) precipitation from C-bearing fluids (Winchel 1911; Alfonso et al. 1995; Luque et al. 1998 and references therein; Long et al. 2013); ii) xenocrystic material, i.e., residual phase inherited from carbonaceous pelitic source rocks (e.g., Broska et al. 1992 and references therein; Kanaris-Sotiriou 1994; Seifert et al. 2010) or assimilated from metasedimentary wall-rocks; iii) metasomatic process involving C-bearing aqueous fluid phases (e.g., Weiss et al. 1981) which may precipitate onto restitic graphite (Duke and Rumble 1986); iv) in carbonatite rocks, breakdown of Fe carbonate with reduction of the carbonate ion (e.g., Rosenberg 1963; Gellantli 1966), or v) precipitation from carbonatite magmas (Doroshkevich et al. 2007). In granitic rocks of peraluminous character (S-type granites), the graphite occurrence is frequently associated to apatite, occurring as solid microinclusions (e.g., “dusky apatite” of Broska et al. 1992, and references therein; Gottesmann and Wirth 1997; Seifert et al. 2010), or as a solid phase in fluid inclusions (e.g., Jaszczak and Trinchillo 2013; Long et al. 2013).

In this study we characterize fluorapatite in the peraluminous and perphosphorous granites from the Variscan Belvís pluton, as part of an ongoing study of its accessory minerals. On the basis of textural, major and trace chemical composition, determined by electron-microprobe (EMP), and laser ablation multicollector inductively coupled plasma mass spectrometry (LA-

ICP-MS), we have characterized three types of magmatic apatite. We also describe a new occurrence of graphite in granitoid rocks, as abundant needle-like inclusions hosted in magmatic fluorapatite. The characteristics of graphite-bearing apatite compared to the other apatite types provide constrains to the origin of this uncommon magmatic graphite occurrence.

Geological setting

The Variscan orogeny generated large granitic batholiths in the inner parts of the Iberian Peninsula (the Central Iberian Zone, CIZ), in an age range from 315 to 295 Ma (Appendix[1] Fig. 1a), which encompasses a significant volume of fractionated plutons (e.g., Villaseca et al. 1998; Orejana et al. 2012; Merino Martínez et al. 2014). The contrasted nature of country rocks as source lithotypes (metasedimentary and metaigneous rocks) would explain two different batholitic lineaments in this area: the Spanish Central System (SCS) and the Montes de Toledo (MT) batholiths, this last in the southern part of the CIZ (Appendix[1] Fig. 1a) (Villaseca et al. 2014). The dominant peraluminous and perphosphorous granitoids of the MT batholith were probably generated from pelitic sources similar to those of the surrounding country rocks, the Schist Greywacke Complex (Villaseca et al. 2008; Merino Martínez et al. 2014), providing a S-type character. The most fractionated and perphosphorous granites of the MT batholith outcrop in the westernmost sector (Villaseca et al. 2008) and, among these, the Belvís pluton stands out. The ca. 3.5 km^2 Belvís pluton is reversely zoned with four biotite and/or muscovite granite units (G1 to G4) showing a foliated fabric (Appendix[1], Fig. 2c and 2d) broadly parallel to the outer contact with the low-grade metasedimentary rocks (Appendix[1] Fig. 1b; Appendix[1] Figs. 2c and 2d). A km-size contact aureole of high grade is developed in the country rock (Merino et al. 2013), along with a secondary schistosity concordant with the plutonic shape, suggesting

120 a dome intrusion (Pérez-Soba et al. 2014). The presence of xenoliths for the whole pluton is
121 very rare.

122 Quartz, K-feldspar, plagioclase, biotite, muscovite and accesory but widespread sillimanite
123 (mainly hosted in most of the magmatic minerals) are the rock-forming minerals in the Belvís
124 granites. Phosphates are common accessory minerals in these granites, including monazite,
125 xenotime, fluorapatite and childrenite-eosphorite. The high U content of monazite, xenotime
126 and zircon and a complex accessory mineral association of gahnite, chrysoberyl and beryl in
127 the Belvís leucogranites have been remarked in previous studies (Orejana et al. 2012; Merino
128 et al. 2013; Pérez-Soba et al. 2014)

129 The chemical composition of the Belvís granites is characterized by their strong
130 peraluminous character (ASI = 1.26 - 1.32), along with high P_2O_5 (up to 0.85 wt%), low CaO
131 (0.26 - 0.56 wt%) and high U (6.8 - 13.5 ppm) contents (Villaseca et al. 2008; Merino et al.
132 2013). The inner units (G3 and G4) display higher FeO, MgO, K_2O, TiO_2, Ba, Zr, Hf, Th, Pb,
133 Y and rare earth elements (REE) contents when compared to the outermost granites (G1 and
134 G2 units), which in turn have higher P_2O_5, Na_2O, Rb, Sr, U, Nb, Ta, F and Li contents (Merino
135 et al. 2013; Pérez-Soba et al. 2014). Zircon from the Belvís pluton gave an accurate
136 emplacement age of 310 ± 4 Ma (Merino Martínez et al. 2014), defining a late-to-post Variscan
137 D3 emplacement (320 to 312 Ma age, e.g. Dias et al. 1998). Estimated *P-T* conditions of pluton
138 emplacement were constrained from 660-695 °C (for G1 pulse) to 725-760 °C (for G4, the last
139 pulse), with pressures in the range of 1.5 to 2 kbar (Merino et al. 2013).

140

141 ## Results

142 The sampling and analytical methods section is available in Appendix[1] Text.

143 ### Apatite petrographic features

144 A petrographic description of Belvís granites can be found in Merino et al. (2014) and
145 Pérez-Soba et al. (2014). Apatite is, along with monazite, the most abundant accessory mineral
146 in the Belvís granites. Three apatite types are distinguished according to textural features
147 (Table 1). Type 1 mainly appears as light green coloured, equant, euhedral (Fig. 1a) to anhedral
148 (Fig. 1b) crystals, ranging from 20 to 2000 μm, although about 90% are smaller than 600 μm.
149 The euhedral and smaller sections mainly appears as inclusions in plagioclase in the most
150 fractionated granites (G1 and G2), whereas the bigger and anhedral sections, ranging from 250
151 to 2000 μm, are rare and mostly found in the less fractionated units (G3 and G4), included in or
152 interstitial to feldspars, quartz and micas. Type 2 and type 3 apatite mostly appear as anhedral
153 crystals. Type 2 is characterized by an irregular dusty appearance, with frequent intragranular
154 cracks (Appendix[1] Fig. 3b, 3c, 3d and 3e; Figs. 1d, 1e and 1f). They appear as large sections
155 (150 -2800 μm), interstitial to the main granite minerals with interlobate shapes (Appendix[1]
156 Fig. 3b, 3c, 3d and 3e; Figs. 1c-1e), although occasional euhedral sections are found. Type 2
157 apatite appears in G2, G3 and G4 units, but lacks in the most evolved G1 unit. It may be locally
158 abundant, especially in the G4 granite (e.g., about 30 crystals in a standard thin section,
159 Appendix[1] Fig.2). SEM images reveal that dusty sectors contain ample acicular graphite
160 microinclusions (Figs. 1f-1h). Most apatite crystals are inclusion free, with the exception of
161 some occasional zircon crystals. Type 3 apatite appears only in the most evolved G1 granite
162 unit, mainly as anhedral (but also subeuhedral) crystals (Fig. 1i), interstitial to the main granite
163 forming minerals, and some crystal reach up to 300 μm. This apatite type appears as feathery
164 aggregate crystals (Fig. 1i, j), oriented (Fig. 1k) or variably oriented in sectors (Figs. 1j and 1l)
165 and includes occasional childrenite-eosphorite (Fig. 1i). However, large childrenite-eosphorite
166 crystals, which usually include tinny apatite, do not show any relationship with the feathery
167 type. Moreover, type 3 apatite has not been observed in the outer part or cracks of other

magmatic phosphates in the Belvís granites. These observations suggest a magmatic origin for this apatite type.

The textural relationships with the main granite minerals and the variable shapes of the three apatite types provide evidence of an overlapping sequential crystallization from type 1 to type 3.

Apatite composition

Representative major and trace element compositions of the three apatite types of the Belvís granites are shown in the Appendix[1] Table1, and their main features are synthesized in Table 1. The three apatite types are fluorapatite: F ranges from 1.87 to 4.31 wt% (overestimated, see analytical methods), with low amounts of Cl (<0.50 wt%) and calculated OH. Most fluorapatite is characterized by high MnO and FeO contents, which display wide ranges (MnO = 0.36 - 4.30 wt%; FeO = 0.04 - 5.09 wt%). In the MnO vs. FeO plot (Fig. 2a) type 1 and type 2 apatite show the same compositional ranges, with FeO/MnO ratio values below 1:2. Apatite with graphite inclusions (type 2), although similar in most of the compositional features to type 1, is richer in Sr, LREE, Zr and Hf contents (Figs. 2b and 2c), and reaches the highest HREE (<2133 ppm) and U (156 – 460 ppm, average of 260 ppm) contents (Fig. 2d). Type-2 apatite shows low Th contents (up to 46 ppm, average of 10.53 ppm) compared to U, although both elements display positive correlation (Fig 3d). The U content of type 1 and type 2 apatite is high when compared to apatite in other felsic granitic rocks, either from alkaline, S- or I-type suites (<235 ppm Zirner et al. 2015; <40 ppm, Belousova et al. 2002; <187 ppm, Hoskin et al. 2000; <184 ppm, Cao et al. 2013; <119 ppm; Mao et al. 2016) (Fig 3d), although lower than data from rare metal-rich highly fractionated granites and LCT pegmatites (e.g., 7404 ppm, Raimbault and Burnol 1998; ca.1000 ppm, Cao et al. 2013) and from a metamorphosed syenite (681 ppm, Mao et al, 2016). The high U content in the apatite is in accordance with its

192 association to exceptional U-rich monazite and xenotime of these Belvís granites (Pérez-Soba
193 et al. 2014). Type 3 apatite composition contrasts by higher FeO_{tot} contents (<5.09 wt%,
194 average of 1.21 wt%) and FeO/MnO ratio values above the 1:1 ratio (Fig. 2a). In addition, type
195 3 is considerably richer (in wt%) in Na_2O (<1.08), Cl (<0.81) (Fig. 2e), and (in ppm) Sr (1596 -
196 2490) (Fig. 2b), Be (<502), Zn (<239) and B (<28) than type 1 and type 2 apatite, which show
197 most contents below detection limits (Appendix[1] Table 1). On the contrary, type 3 shows the
198 lowest P and Ca contents, low analytical totals (Fig. 2f) and extremely low Y, REE (Fig. 3a), U
199 and Th contents (Fig. 2d). Most apatite crystals show no evidence of zoning in BSE imaging,
200 and those euhedral to subeuhedral crystals with slight zoning do not show systematic core-rim
201 chemical variation.

202 Li content of the three types show similar range (9 – 104 ppm, average of 39 ppm, Table 1
203 and Appendix[1] Table 1). Comprehensive data of Li content in apatite are scarce in the literature
204 but these data (e.g., 2.1 ± 0.9 ppm averaged in apatite from felsic rocks, Piccoli and Candela
205 2002) indicate that Belvís apatite is Li-enriched. Electron energy loss (EEL) spectra performed
206 in the three apatite types does not detected carbon. None of the analyzed nanosamples have
207 absorption K-edge peaks around 284 eV, corresponding to the existence of amorphous carbon
208 in EELS, or around 290 eV (with a second broader peak centered at 302 ev) corresponding to
209 the carbon-edges in carbonates.

210 The REE content in apatite of the Belvís granites is largely variable (0.5–5878 ppm) (Table
211 1 and Appendix[1] Table 1). Type 1 and type 2 apatite show a wide REE total contents (1118–
212 5878 ppm), even at sample scale, displaying positive correlation between LREE (2131–4048
213 ppm) and HREE+Y contents (297–2133 ppm) (Fig. 3a). Type 1 apatite displays broad and
214 continuous chondrite-normalized REE patterns with a significant dissociation between LREE
215 and HREE b: the LREE pattern varies from regular and negative sloped pattern to a flat and

irregular one ($(La/Sm)_N$ = 1.91–6.06) (Fig. 3b), whereas the HREE show a consistent negative slope ($(Gd/Lu)_N$ = 1.7–4.9) with a constant third tetrad effect (1.25–1.42, with the exception of one sample having a 2.2 value). Type 2 apatite shows consistent planar LREE patterns and negative fractionated HREE trend, this last similar to type 1, with a tendency to be HREE enriched (Fig. 3c). In both apatite types, the negative Eu anomaly increases (from 0.79 to 0.07) displaying positive correlation with the total REE content and the REE fractionation $(La/Yb)_N$ (Fig. 3d). The chondrite-normalized patterns of both apatite types show different anomalies: a low negative Nd anomaly (0.76–0.94), a weak positive Ce anomaly (1.06–2.19, more pronounced in type 2 apatite) and a mostly slight positive Yb anomaly (0.97–1.17). Type 3 apatite shows REE contents mostly below detection limits, 3 to 4 orders of magnitude lower than those from type 1 and type 2. In order to compare with the other apatite types, chondrite normalized REE patterns of type 3 are estimated using the highest content just above the detection limits (Fig. 3c).

Most of the described compositional features of type 1 and type 2 apatite are typical of S-type granites (Sha and Chappell 1999; Broska et al. 2002, 2004). However, some differences can be highlighted: i) the three apatite types are, on average, richer in Mn and Fe than those from S-type granites, and even richer than apatite from specialized S-type granites (e.g. Broska et al 2002); ii) type 1 and type 2 apatite from Belvís are considerably richer in U than typical apatite from I or S-type granites (Fig. 2d); iii) they have higher LREE and lower HREE contents than apatite from other S-type (Sha and Chappel 1999) or peraluminous granites (Chu et al. 2009); iv) LREE/HREE ratio in Belvís apatite (1.6 - 4.9) is more characteristic of apatite from mafic I-type granites than from S-types (Sha and Chappell 1999), so in chondrite-normalized REE spectra the HREE pattern show an atypical negative slope; v) the extremely

low Eu negative anomaly in some of the studied type 1 apatite crystals are uncommon in S-type granites (Sha and Chappell 1999).

Graphite microinclusions

Petrographic features. Graphite inclusions are abundant (up to 10 vol% of apatite crystal), displaying a broad alignment (Fig. 1f) or randomly arranged within the apatite crystals (Fig. 1g, h), in both cases heterogeneously grouped in clusters. Secondary electron images show that these graphite inclusions are filaments (Figs. 4a and 4b) with diameters about 1 μm (Figs. 4c and 4d) and lengths observed of 15 μm (Fig. 1g), and conformed by graphene sheets bonded to each other in a stacked sequence. It is remarkable the systematic presence of a cavity around each graphite inclusion with similar contour that the graphite shape and lengths exceeding in about one third that of the related flake graphite (Figs. 4c and 4d).

Graphite inclusions in igneous minerals commonly appear as flakes, and have never been described with crystalline habits typical of graphite crystallized from fluids as, e.g., spherules (Duke and Rumble 1986; Luque et al. 2012). Two previous descriptions of graphite microinclusions within magmatic apatite were recorded in peraluminous leucogranites from the Bohemian Massif: Broska et al. (1992) studied dusky apatite in Variscan leucogranite massifs of the Western Carpathians caused by the presence of "fine graphite flakes"*;* Seifert et al. (2010) reported in the Caledonian S-type Rumburk granite disperse graphite (associated to other minerals) as microinclusions (up to 3 μm) in apatite and other minerals or as "interstitial flakes". Other references of graphite in igneous rocks are from Montanini et al. (2010), which found graphite as "dispersed flakes and stacks of flakes" (up to 2–3 mm) in garnet pyroxenite layers from the Northern Apennines; Kvasnitsa et al. (1999) described in anorthosites different textures of graphite interstitial to plagioclase, which display a complete transition from "tabular

263 flakes to columnar individuals, in a sorter (sic) of macrospiral growths with pseudo-
264 dipyramidal terminations". Patel and Deshapande (1970) found some graphite filaments (65–
265 125 μm) with c-axis planes oriented along the fiber length, growing from graphite crystals of
266 the Ticonderoga graphite mine. Among graphite shapes found in literature, this last graphite
267 morphology is the most similar to those described here, although significantly longer than the
268 15 μm observed in graphite of Belvís.

269 The systematic occurrence of a cavity around graphite inclusions (Figs. 4c and 4d) could be
270 interpreted as a contraction. It is known that low irradiation dose causes the graphite to shrink
271 parallel to the layer planes (a-axis direction) (Burchell 1997). The high U contents of type 2
272 apatite (up to 450 ppm, Appendix[1] Table 1), exceptionally high for common granite rocks,
273 could be a natural source of the radiation.

274 **Chemical characterization.** Identification of graphite has been successively carried out by
275 EMP line analysis, EDX spectra and elemental X-ray maps. Figure 5 shows two EDS line
276 analysis on graphite microinclusions in type 2 apatite for C, Ca, P and F, which systematically
277 reveal that P, Ca and F contents define sharp falls within rich-inclusion areas while carbon
278 defines a peak.

279 **Carbon isotope composition.** Carbon isotope composition of bulk rocks have been
280 obtained from the wall rocks (SGC pelitic metasediments), nearby granites of the MT batholith
281 (Navalmoral de la Mata pluton) and the Belvis granites (Table 2). Carbon isotope ratios ($\delta^{13}C$
282 in ‰) from the graphite-bearing Belvís granites range from –24.4 to –27.4 indicating a
283 biogenic carbon source (Fig. 6). These values are within the wide range of ratios shown by
284 metapelitic rocks from the CIZ (Fig. 6), although slightly higher than the nearest
285 metasedimentary wall-rocks (–31.00 to –32.49). Moreover, Belvís granites have also similar

but slightly higher $\delta^{13}C$ values than other graphite no-bearing peraluminous granites of the MT batholith (N. Mata granites: –29.24 to –32.78). Carbon isotope composition of the Belvís granites suggests an organic carbon derivation inherited from the metasedimentary source.

Discussion

Substitution mechanisms

Composition of apatite can be described by the common structural formula $M1_4\,M2_6\,(TO_4)_3\,X$ (Pasero et al. 2010). T includes cations with more than 4-fold coordination (P^{5+}, As^{5+}, V^{5+}, Si^{4+}, S^{6+}). The X anionic site is occupied by monovalent anions (F^-, Cl^-, OH^-), which can substitute for each other resulting in almost a complete range of substitution between the three end-members of apatite; moreover, vacancies (e.g., Piccoli and Candela 2002), H_2O molecules, and divalent anions (O^{2-}, CO_3^{2-}) can substitute in this channel site (e.g., Pasero et al. 2010). M-site (Ca^{2+}) accommodates cations in two non-equivalent, symmetrically and crystallographically distinct sites: the 9-fold coordinated site (M1 or Ca1, larger in size and with trigonal symmetry) and the 7-fold coordinated one (M2 or Ca2, smaller and lower in symmetry, surrounded by one F atom) (e.g., Pasero et al. 2010). Large divalent (Ca, Pb, Ba, Sr, Mn, Mg, Fe), trivalent (REE, Y, Al, Bi) or monovalent (Na, Li) alkaline earth-element cations substitute over M1 and M2 sites. The ability of apatite structure to accommodate this broad spectrum of different cations and anions depends on several factors: ionic size, redox conditions, coordination preferences of the substituting cation, temperature, etc. (e.g., Hughes et al. 1991; Pasero et al. 2010; Wopenka and Pasteris 2005).

In the Belvís apatite the T-position is occupied mainly by phosphorous, with occasional analyses with Si content above detection limit. Phosphorous content only displays a broad negative correlation with the Ca content but does not correlate with any of the other analyzed

not essential structural cations (not ESC) (as Mn, Fe, Mg, Sr, Na, Al, REE, Y, Th and U), , suggesting that it may be involved in coupled substitution mechanisms. The X-site is dominated by F, with traces of Cl. The occupancy of this site is below full capacity (2 atoms per formula unit (apfu) about 3.7 wt%, de Toledo et al. 2004). This deficiency could be related to the existence of structural OH^- (McClellan and Lehr 1969) or vacancies (Pan and Fleet 2002) in this site. In type 1 and type 2 the F content only displays correlation with the OH^- content (estimated by charge balance). The estimated values of OH^- do not systematically correlate with excess of oxygen analyzed by EMP in the respective analysis (see analytical methods), suggesting, that vacancies may be included in this OH^- estimation. The F content in type 3 apatite shows a positive correlation with the Ca contents (Figs. 7a and 7b), suggesting some substitution mechanism involving both F and Ca. These elements participate in several coupled mechanisms, all of them with associated vacancies (Pan and Fleet 2002, and references therein), which may explain the low anion occupancy observed in this apatite type. The F content displays broad negative correlation with the Cl contents of type 3 apatite. This F-Cl correlation may be explained by changes in the *P-T* conditions (e.g., Harlov 2015; Webster and Piccoli 2015) or competition with other Cl-bearing minerals (e.g., Harlov 2015). In the Belvís granites, muscovite or biotite show extremely low Cl contents (Merino 2014), and the four granite units intruded in a short time span at the same emplacement level. Therefore, the significant higher Cl content in type 3 apatite rather suggests a significant melt compositional change (e.g., enrichment in fluxing components) in the last magmatic stage that this apatite type records, as also would evidence the good positive correlation of Cl with Na (Fig. 2e), Li (Fig. 7c), Be and B contents.

Among the monovalent cations that potentially substitutes for Ca, only Na and Li show significant values in the Belvís apatite. In type 1 and type 2 Li shows positive correlation with

both LREE and Y+HREE contents (Fig. 7d), so Li incorporation could be explained via the coupled substitution: $Li^{+} + (Y+REE)^{3+} = 2Ca^{2+}$. A similar mechanism was proposed by Pan and Fleet (2002) and Harlov et al. (2002), although involving Na as the monovalent cation, which, on the other hand, in the studied apatite is not evident. In type 3 apatite, in wich Na content is particularly high, this cation only show a remarkable positive correlation with Cl, Li (Figs. 2e and 6e) and Fe contents (Fig. 7f). The correlation between Na and Fe may suggest a charge compensated substitution mechanism of Fe^{3+} and Na^{+} for Ca^{2+} (Pan and Fleet 2002). Therefore, Na would have been incorporated in type 3 apatite as long as Fe^{3+} was present, and possibly favored by the high Cl and Li contents. In type 3 apatite Li is negatively correlated with F, indicating Li could be likely incorporated via the coupled substitution mechanism: $Li^{+} + \square = Ca^{2+} + F^{-}$ (Pan and Fleet 2002). In short, in type 3 apatite the strong correlation displayed between Cl, Fe^{3+}, Li, Na, Be and B suggests the involvement of a residual fraction of magmatic melt rich in fluxing components and with higher oxidation state compared to that related with the type 1 and type 2 apatite.

In the studied three apatite types, Fe^{2+} and Mn^{2+} are the main cations for Ca substitution. The good correlations between them suggest a simple mechanism for Fe and Mn incorporation: $(Fe^{2+} + Mn^{2+}) = Ca^{2+}$ (e.g., Pan and Fleet 2002; Harlov et al. 2006). Other divalent cations, as Sr, Mg or Be, where above detection limits (mostly in type 3, Appendix[1] Table 1), are negatively correlated with Ca.

Unlike divalent cations which substitute for Ca without variation of the apatite structure, the incorporation of M^{3+} cations requires a coupled substitution in which they substitute for Ca^{2+} and P^{5+} as long as Si^{4+}, Na^{+} or vacancies are involved (Fleet and Pan 1995). In type 1 and type 2 apatite the M^{3+} involving cations are REE^{3+}, Y and Al^{3+}, which do not show distinct correlations with any other substituting cation. This reduces the substituting mechanisms to this

one: $2REE^{3+} + \square = 3Ca^{2+}$ (cf. Elliot 1994). In the case of type 3 apatite, the extremely low REE and Y contents are likely explained from local crystallization of REE-exhausted melts, although their relatively high Cl content could also decrease the uptake of REE in fluorapatite (Fleet et al. 2000).

Tetravalent cations U and Th are only significant in type 1 and type 2 apatite (Appendix[1] Table 1), displaying positive and good correlation between them (Fig. 2d). They can substitute for Ca via a Ca-deficiency mechanism, such as vacancies or coupled substitutions involving Na or Si (Luo et al. 2009, and references therein). As the incorporation of U in the fluorapatite structure is in the tetravalent state (Luo et al. 2009) and in the Belvís apatite samples the (Th + U) content is not correlated with Na or Si, the most plausible mechanism is to charge balance generating vacancies: $(U + Th)^{4+} + \square = 2Ca^{2+}$.

Type 3 apatite shows systematically low analytical totals (Appendix[1] Table1, Fig. 2f). Specific references on low analytical totals in apatite from igneous rocks are very scarce in literature (e.g., de Toledo et al. 2004). In general, low totals have been ascribed to weathering effect, porosity by partial dissolution or possible compounds not analyzed. In a profile of variably weathered carbonatitic complex, de Toledo et al. (2004) correlated low analytical totals with: (a) loss of substituting cations for Ca, (b) increase of substituting anion (carbonate) for P, (c) the increase of F, and (d) increasing CaO/P_2O_5 ratio. In our case, analytical data (LA-ICPMS) on type 3 apatite type show trace contents of substituting cations, and the EEL spectrometry has not detected carbon. Therefore, we consider that low totals of this type 3 apatite may be explained by the microporosity of the surface roughness associated to its feathered texture, which, according to Sorbier et al. (2004), can introduce large quantification errors if a contaminant (e.g., carbon during sample preparation) is not analyzed.

382 **Constrains on the fluorapatite crystallization**

383 Textural features of type 1 apatite from Belvís units suggest a broad crystallization stage
384 evolving from euhedral crystals, included in early rock-forming plagioclase, to anhedral and
385 bigger crystals, included in later rock-forming quartz, micas and K-feldspar. The most frequent
386 interstitial position of type 2 apatite would indicate a widespread later crystallization with
387 respect to type 1 crystals. Whole-rock chemical evolution from G4 to G1 granites shows the
388 typical trends of highly-fractionated, P-rich and Ca-poor S-type granites, with P_2O_5 and MnO
389 increase, and CaO, FeO and REE contents decrease (e.g., London et al. 1993). However apatite
390 composition does not correlate with whole-rock MnO or FeO contents of the corresponding
391 sample, or other whole-rock evolutionary parameters (e.g., ASI, TiO_2 or SiO_2 contents),
392 suggesting that apatite characterizes the last sequence of magmatic evolution in these residual
393 melts. Moreover, the fact that in the same thin section apatite may display significant variations
394 or appear near to other apatite type could evidence the melt drop-like compartmentalization of
395 highly residual melts. The decrease of apatite amount from G4 to G1 granites may be explained
396 by a lower P availability, as increasing phosphorous partition into K-feldspar and plagioclase
397 via the berlinite substitution is shown by the Belvís granites (Table 1 of Villaseca et al. 2008).

398 The lack of chemical zoning in type 1 and type 2 apatite may provide further information
399 about crystallization conditions. In theses cases, the rate of crystal growth is lower than the rate
400 at which elements in the melt diffuse (Kuehner and Joswiak 1996), or apatite crystallization
401 temperatures above 500 °C could erase the zoning, as a result of diffusive equilibration of Mn
402 during or after crystallization (Cherniak 2005; Sirbescu et al. 2009). Temperatures of
403 crystallization in the Belvís granites were estimated about 700°C (Merino et al. 2013), although
404 lower temperatures could be reached because the relatively late apatite crystallization and the
405 presence of fluxing components in melts could decrease granite solidus temperatures,

406 favouring undercooling conditions. In addition, in these highly fractionated and P-F-rich melts
407 a strong increase of cation and volatile diffusion rates is reasonable to expect (e.g., Hannah and
408 Stein 1990; Holzt et al. 1993; London et al. 1993). Therefore, undercooling conditions coupled
409 with high cation diffusion may result in unzoned apatite crystals.

410 Low oxygen fugacity is characteristic of S-type magmas (e.g., Sha and Chappell 1999).
411 Some evidences of low oxidation state in magmas deduced from apatite composition are: i) Fe,
412 Mn or U substituting for Ca are indicative of divalent charge (Fe^{2+}, Mn^{2+}) or tetravalent charge
413 (U^{4+}) (e.g., Belousova et al. 2002; Buda and Pál-Molnár 2012; Miles et al. 2014) ; ii) low
414 oxygen fugacity enhances Eu^{2+}/Eu^{3+} ratio in the melt, resulting in higher negative Eu anomaly
415 in the chondrite-normalized apatite REE patterns as Eu^{3+}, with similar ionic radius than Ca, is
416 preferred by the apatite structure (Roeder et al. 1987; Sha and Chappel 1999; Broska et al.
417 2002; Cao et al. 2011); iii) in the same way, a positive Ce-anomaly could be explained by
418 reduced state of Ce (as Ce^{3+}). Pan et al. (2016) propose bivariant plots of elements with
419 opposite partitioning behavior in changing oxidation state during magma crystallization.
420 Following this assumption, Eu/Eu* or Ce/Ce* could define the oxidation state during the
421 growing of the three apatite types, as it is shown in Figure 8a. In this plot, type 1 apatite defines
422 a broad negative correlation, possibly recording more variable oxygen fugacity conditions,
423 whereas type 2 plots in low fO_2 fields, and type 3 apatite display scattered trends at higher
424 oxygen fugacity. The high negative Eu anomaly in chondrite normalized REE patterns of type
425 2 apatite would corroborate a low oxidation state. However, in a single thin section type 1
426 apatite shows strong variations of the Eu and Ce anomalies, suggesting that other factors, in
427 addition of redox conditions or independent of this, could explain these variations. Some
428 studies have shown that the Eu anomaly in accessory minerals may result for previously Eu

depleted melt, either from the source (e.g., Rubatto 2002), after plagioclase crystallization (e.g., Hoskin et al. 2000) or by co-crystallization with K-feldspar (Murali et al. 1983).

Apatite chemistry may be interpreted according to whole-rock melt composition (Prowatke and Klemme 2006; Cicconi et al. 2012), REE preferences of coevally crystallizing accessory minerals (e.g., Bea 1996; Procházka and Matějka 2006; Miles et al. 2013) or other factors (e.g., redox conditions). As apatite chemistry is not correlated with the Belvís granite whole rock composition, we consider that competition with other mineral phases may control REE apatite compositional variations. The monazite crystallization would explain that apatite composition displays a trend of variable Y but constant low Ce contents (e.g., Sha and Chappell, 1999; Chu et al. 2009; Miles et al. 2013). In similar plots, (e.g., LREE vs. Y+HREE), type 1 apatite shows a positive correlation whereas type 2 does not (Fig. 8b). These differences are also evident in the plot $(La/Sm)_N$ vs. (Y + HREE) (Fig. 8c), where type 1 apatite records a variable competition with other LREE and HREE-bearing phosphates (monazite and xenotime), whereas type 2 exclusively nucleated and grew from relatively enriched LREE melts, regardless of HREE-Y content.

Textural and compositional features of type 3 apatite define a change in the magmatic conditions in the more evolved unit of the Belvís pluton, where it has only found, compared to those deduced from previous apatite types. The common subhedral to anhedral crystals are conformed by feather aggregates which evidence a self-assembly mechanism of growing (Penn 2004), typically involving a fast nucleation followed by aggregation growth, in this case in a disordered way. The high number of nuclei and their small size would evidence crystallization under high undercooling conditions, i.e., temperature varies more rapidly than nuclei grow. As type 3 crystal shapes are sharp and with no evidences of reaction with type 1 apatite (type 2 and type 3 do not occur in the same pluton unit), different apatite growth conditions are

453 involved. The highly evolved composition and the external location of the G1 unit within the
454 pluton may provide appropriate conditions for partial loss of volatiles (or fluxing components),
455 which would contribute to a higher undercooling (Hort 1998). On the other way, higher oxygen
456 fugacity during late crystallization stages can be deduced in the residual melts of the G1 unit,
457 on the basis of both graphite-bearing apatite absence and high Fe^{3+} contents in type 3 apatite
458 composition. Strong $Fe^{3+}/\sum Fe$ increases have been observed during devolatization process in
459 hydrous rhyolite magmas by loss of H_2 or H_2O during the ascent at shallow levels (Humphreys
460 et al. 2015). The previous crystallization of Cl-poor type 1 and 2 apatite would enhance Cl
461 activity in the last fractions of the residual melts, favoring relatively Cl-Na-Li-Be-Fe^{3+}-rich and
462 REE-exhausted minor melts, from which type 3 apatite would crystallize.
463 *P-T* conditions for the crystallization of apatite could be estimated by calculating apatite
464 saturation temperatures using the experimental model of Piccoli and Candela (1994), modified
465 from Harrison and Watson (1984), according to SiO_2 and P_2O_5 whole-rock composition. The
466 main objection for using this equation in these peraluminous and perphosphorous granites is
467 the complex estimation of the P_2O_5 content for apatite saturation, since feldspars, but also
468 micas and cordierite, are P-bearing phases in perphosphorous leucogranites, as it is the case of
469 the Belvís granites. So we consider a better proxy the *P-T* conditions calculated by Merino
470 (2014) and Merino et al. (2013) on the basis of Ti-in-zircon and mineral paragenesis for the
471 central Belvís units (G4 and G3 leucogranites), providing *P* about 2 kbar, and *T* up to 750 °C.
472 The estimated lately crystallization for type-3 apatite and the probable higher fluxing contents
473 might indicate significantly lower temperatures.
474

475 **Origin of graphite in the Belvís granites**

476 The origin of studied graphite is discussed by comparison with previous studies in magmatic
477 rocks:

478 1. Graphite as interstitial flakes or included in rock-forming minerals has been interpreted
479 as restitic in origin, as this mineral behaves as refractory during anatectic melting processes of
480 metasedimentary protoliths (e.g., Broska et al. 1992, Seifert et al. 2010). Restitic graphite could
481 also be related to assimilation of metasedimentary wall-rocks (Duke and Rumble 1986). The
482 carbon isotope composition of the Belvís granites support that the studied graphite has an
483 inherited biogenic origin (Fig. 6). Although graphite as xenocryst would be plausible in the S-
484 type Belvís pluton, graphite in these granites occurs exclusively as euhedral filaments hosted in
485 magmatic fluorapatite, suggesting that carbon may be present in the residual melts as graphene
486 units growing later as acicular crystals. The rare occurrence of metasedimentary xenoliths,
487 coupled with the higher carbon isotopic composition of the Belvís granites compared to the
488 wall-rocks metasediments, make it unlikely a xenocrystic origin for graphite. Moreover, in the
489 MT batholith graphite has been only found in the highly fractionated Belvís pluton. Therefore,
490 it appears unlikely that more mafic and restite-rich granitic units of this large batholith lack
491 graphite if this were strictly restitic.

492 2. Carbon mobilized by hydrothermal fluids from the protoliths or wall-rocks (as carbonate
493 or organic-rich sediments) during high temperature events (contact metamorphism, anatexis)
494 would precipitate in the granitic melts as fluid inclusions within rock-forming minerals, with
495 graphite as daughter crystals (Winchel 1911; Duke and Rumble 1986; Alfonso et al. 1995;
496 Long et al. 2013). In the Belvís granites, C has only been observed as graphitic micro-
497 inclusions hosted by magmatic apatite.

498 3. Carbon content in apatite may reach significant values (Comodi et al. 2001; Brigatti et al.
499 2004) after carbon substitution at high temperatures, and this carbon may be lately exsolved as

graphite inclusions during cooling. In the apatite structure carbon substitution in the phosphate site is probably operative in the form of CO_3 and less frequently in the anion-site for $(OH)^-$ (e.g., Freund 1986; Peck and Tumpane 2007; Yi et al. 2013). The shape of the graphite inclusions in the Belvís apatite, their wide range of grain size and their heterogeneous distribution, either parallel or randomly orientated, are not characteristics of a network of crystallographic-oriented crystals (Figs. 1f-1h). Moreover, EEL analyses do not detect carbon in any of the apatite types.

4. Co-crystallization of apatite and graphite similarly Gottesmann and Wirth (1997) proposed for pyrrhotite inclusions in apatite from granitic rocks. These authors observed rhythmical disposition of pyrrhotite normal to the c-axis of apatite crystals. They proposed that pyrrhotite nuclei would have precipitated in the interface apatite-melt according to changes of Fe and S contents in the melt, and favored by similar lattice spacing between them. In some of the studied apatite crystals graphite inclusions show a preferred orientation (Fig. 1f) but do not define a rhythmical disposition.

The model of simultaneous growth of fluorapatite and graphite from highly differentiated granite melts is considered the most plausible origin for the studied graphite inclusions, as we discuss below.

In the MT batholith the presence of graphite is limited to the most highly fractionated (P-F-Li-Be-Rb-U-Cs-rich) pluton, and has only been observed as microinclusions within fluorapatite. This suggests a strong association of P, F and C related to magma source signatures due to the metasedimentary derivation of these granites (Villaseca et al. 2008; Merino et al. 2013, 2014). High carbon solubility in apatite has been previously noted (e.g., Jahnke 1984; Regnier 1994). Besides the association of P-C-F, another factor might have contributed to graphite occurrence since type 1 apatite, compositionally similar to type 2, does

not include graphite. Type 2 differs from type 1 apatite mainly by having slightly higher LREE-Zr-Sr contents. These differences suggest that C was favorably partitioned into residual fractions of P-rich melt, with relative high REE-U contents (but not enough to stabilize monazite) together with adequate Ca contents to form apatite.

Type 2 apatite mostly appears as interlobated crystals in interstitial position (Figs. 1c-1e). This texture resembles those developed between immiscible melts preserved by rapid cooling rates. On average, the fluorapatite-graphite crystals are made up of 90% fluorapatite and 10% graphite, so a broad estimation on the basis of fluorapatite composition shows that high concentration of volatile and fluxing components (around 30 wt%) has to be achieved in these melt droplets: 18 wt% P + 10 wt% C + 2 wt% F + (Li + Cl + OH) traces. This fluxing-rich residual melt fraction could suggest melt-melt immiscibility behavior with the silicate melt. In igneous systems the silicate immiscibility with salt melts (fluoride, phosphate, chloride, carbonates and sulphate) has been extensively studied (e.g., Dawson 1962). Phosphorous immiscibility in highly evolved silicate melts was shown early (e.g., Rutherford 1974), although later studies have triggered a controversy as many compositional factors control P behavior in silicate melts, which makes difficult to constrain the final ability of P to be immiscible (Roda-Robles et al. 2012 and references there in). Studies in pegmatite bodies show P-rich segregates (e.g., nodules, Roda-Robles et al. 2012; patches, Thomas and Davidson 2013), therefore some degree of immiscibility can be achieved in the late stage of highly evolved melts, whatever the process or conditions for concentrate P. Graphite is typically a residual phase that remains in the residuum during a crustal partial melting process, but if a small proportion enters in the molten fraction, it would behave as a highly incompatible component. Therefore, carbon content will increase towards residual highly fractionated granite melt. However, carbon itself has low solubility in silicate melts and could be easily lost

548 in epizonal intrusions (as the Belvís pluton is). Therefore, C should be retained in melt for
549 graphite crystallization, and we consider it was most likely associated to these P-F-rich melts,
550 which might enhance the immiscibility character of melt droplets, similarly to immiscibility
551 process in carbonate-silicate liquid systems (e.g. Brooker and Kjarsgaard 2011). Fluorine is
552 highly soluble in hydrous aluminosilicate melts, acting as a fluxing component, apparently
553 more important than P (e.g. Dingwell et al. 1993), but combined with other fluxing components
554 (e.g. Li, B) to explain the viscosity observed in natural systems (Bartels et al. 2013).
555 We consider that in the succession of magmatic pulses forming the Belvís pluton, when
556 most of the granite magma was crystallized, the occurrence of minor volumes of residual P-C-
557 F-(Li)-rich melt fraction could induce an immiscible character, as it is shown for pegmatite
558 systems (e.g., Veksler et al. 2002; Thomas and Davidson 2007) or deduced from pegmatitic
559 phosphate bodies studies (e.g., Roda-Robles et al. 2012; Miles et al. 2013), triggering an
560 emulsion with droplets dimensions (e.g., Thomas and Davidson 2007; Peretyazhko et al. 2007)
561 . Although low temperatures may induce high viscosity in evolved silicate melts, local
562 saturation of fluxing components can be achieved (Bacon 1989). A high initial water content
563 (7-8 w% H_2O, Strong 1988) allows peraluminous melts to reach high degrees of crystallization
564 before water-saturation is achieved and favoring a higher enrichment of incompatible elements
565 in the residual melts and coexisting exsolving fluids (Candela 1989). Although interstitial melt
566 droplets may crystallize at low temperatures, the elevated content in fluxing components would
567 reduce its density and viscosity, increasing the cation diffusion rates and inhibiting zoning
568 textures in the apatite. Decreasing temperatures and fO_2 in an isobaric cooling system could
569 create favorable conditions for graphite precipitation (Frezzotti et al 1994). Therefore, carbon
570 would nucleate as graphite, heterogeneously distributed, and growing either randomly or
571 oriented. Graphite inclusions do not show textural changes in apatite from the G2 to G4 granite

572 units, suggesting that within type-2 apatite carbon supersaturated condition was achieved in
573 these microdomains. In this type of immiscible systems, REE and other incompatible cations
574 tend to be preferentially partitioned into the non-silicate melt (Veksler et al. 2012), which
575 would explain the higher contents in some of these elements such as U, REE, Sr and Zr in type
576 2 apatite, leaving behind a residual melt highly impoverished in these elements. Finally, the
577 shape of graphite inclusions could reflect strong undercooling in these microdomains,
578 enhancing graphite growth as acicular crystals. The peraluminous nature of the Belvís magmas,
579 in addition to their P-rich contents, may delay considerably the apatite crystallization and
580 favour the origin of different apatite generations in local highly fractionated and fluxing
581 element-rich fractions.
582
583 **Implications**
584 The carbon incorporation in granite peraluminous melts from their metasedimentary sources
585 opens a discussion on the carbon behavior during magma evolution while carbon concentrates
586 in the ultimate residual melts (highly fractionated granites and pegmatites), so it questions the
587 way it was transported in an evolving highly polymerized melt framework. Another question is
588 in which conditions graphite from the metasedimentary source is incorporated as a restite phase
589 into the melt and in which allotrope form is maintained during magma evolution until it is
590 stacked as graphene co-crystallizing with granitic apatite.
591 This study provides a singular case of magmatic graphite with fluorapatite in peraluminous
592 granites, which might not be accidental. Fluxing elements as P-F-H, related to the organic
593 matter, have a crucial role as ligands to carbon. Melt species with P-F-C bonds would probably
594 promote melt immiscibility in high-silica magmas. This is a field to be explored in future.
595

Conclusions

1. Three different Fe-Mn-rich fluorapatite types crystallized in the late stages of crystallization of the perphosphorous Belvís granites. Textural and compositional ranges of type 1 and type 2 apatite provide evidences of sequentially overlap with subtle compositional differences between them, whereas type 3 apatite defines later and contrasted conditions of crystallization. The compositional variations do not correlate with whole-rock contents, reflecting the decoupling between conditions of whole-rock features and those of the late accessory minerals. Type 1 and type 2 apatite record low oxygen fugacity, crystallization in high undercooling conditions from highly fractionated residual melts, compositionally similar but with significant higher LREE and Sr contents for type 2 apatite.

2. Type 3 apatite shows an unusual feathered aggregate texture and compositionally is extremely low in REE-Y-Th-U contents, whereas it is relatively rich in Cl-Na-Fe^{3+}-Be-B-(Zn). These features are interpreted as being related to crystallization from highly fractionated residual melts at high undercooling and oxygen fugacity conditions in a late magmatic stage.

3. Inclusion of acicular graphite in type 2 apatite is explained by co-crystallization in melt drops saturated in volatile and fluxing components (P-F-C-H), segregated from highly fractionated (perphosphorous and peraluminous) melts by immiscibility process. This volatile-enriched segregate appeared in relatively LREE- and Sr-undepleted melt fractions. Therefore, the previous monazite crystallization is determinant of the LREE content of apatite. Another factor for graphite crystallization is the strong affinity between volatile and fluxing components in S-type magmas [P-F-(Li-OH)] and carbon (from the metapelitic source). Carbon in these residual melts could trigger immiscibility behavior respect to silicate-rich melt fraction. Fluorapatite and graphite co-crystallized from immiscible melt droplets with high cation diffusivity promoted by the low viscosity related to the high concentration in fluxing

components. This scenario provides conditions for unzoned crystals as well as unusual graphite growth as filaments. The occurrence of graphite in felsic magmas, to our knowledge, is restricted to xenocrysts in peraluminous and P-rich granites. This is the first study assigning a magmatic crystallization for graphite in a granite melt.

4. Local limitations of cation diffusivity by competition with other phase minerals in microdomains of residual melts question the use of chondrite-normalized apatite REE patterns as accurate granite petrogenesis features. On the contrary, detailed studies of compositional variations in apatite and associated minerals may provide more accurate petrogenetic interpretations of the late crystallization history of granite magmas.

Acknowledgements

We are grateful to Javier García for the sample preparation and his assistance with the EEL spectroscopy, and to Ana Vicente and Ángel Mazarios for the efficient advice and assistance during the SEM sessions, from the Centro Nacional de Microscopía Electrónica. Teresa Jeffries and Sonia García de Madinabeitia are thanked for support the LA-ICP-MS sessions, in the Core Research laboratories of the Natural History Museum of London (UK) and in the Geochronology and Isotope Geochemistry-SGIker facility of the University of the Basque Country (Spain), respectively. We thank Clemente Recio and his team, from the Laboratorio de Isótopos Estables de la USAL, for their diligent work. Encarnación Roda-Robles reviewed an earlier version of the manuscript, which considerably improved the discussion and the clarity of descriptions. We appreciate the helpful reviews provided by Dominic Papineau and an anonymous reviewer. This research received support from the SYNTHESYS Project (http://www.synthesys.info/), which is financed by European Community Research Infrastructure Action under the FP7 "Capacities" Program. This work is included in the

644 objectives of, and supported by, the CGL2012-32822 project of the Ministerio de Economía y
645 Competitividad de España, and the 910492 UCM project.

646

References cited

Alfonso, P., Corbella, M., and Melgarejo, J.C. (1995) Nb-Ta-Minerals from the Cap de Creus pegmatite field, Easter Pyrenees: distribution and geochemical trends. Mineralogy and Petrology, 55, 53–69.

Bacon, C.R. (1989) Crystallization of accessory phases in magmas by local saturation adjacent to phenocrysts. Geochimica et Cosmochimica Acta, 53, 1055–1066.

Bartels, A., Behrens, H., Holtz, F., Schmidt, B.C., Fechtelkorn, M., Knipping, J., Crede, L., Baasner, A., and Pukallus, N. (2013) The effect of fluorine, boron and phosphorus on the viscosity of pegmatite forming melts. Chemical Geology, 346, 184–198.

Bea, F. (1996) Residence of REE, Y, Th and U in granites and crustal protoliths; Implications for the chemistry of crustal melts. Journal of Petrology, 37, 521–552.

Belousova, E.A., Griffin, W.L., O'Reilly, S.Y., and Fisher, N.I. (2002) Apatite as an indicator mineral exploration: trace-element compositions and their relationship to host rock type. Journal of Geochemical Exploration, 76, 45–69.

Brigatti, M.F., Malfererrari, D., Medici, L., Ottolini, L., and Poppi, L. (2004) Crystal chemistry of apatites from the Tapira carbonatite complex, Brazil. European Journal of Mineralogy, 16, 677–685.

671 Brooker, R.A., and Kjarsgaard, B.A. (2011) Silicate–carbonate liquid immiscibility and phase
672 relations in the system SiO_2–Na_2O–Al_2O_3–CaO–CO_2 at 0.1–2.5 GPa with applications to
673 carbonatite genesis. Journal of Petrology, 52, 1281–1305.
674
675 Broska, I., Dikov, Y.P., Čelková, A., and Mokhov, A.V. (1992) Dusky apatite from Variscan
676 granitoids of the Western Carpathians. Geologica Carpathica, 43, 195–198.
677
678 Broska, I., Williams, C.T., Aubin, A., Uher, P., and Leichmann, J. (2002) Apatite composition
679 and estimation of fluorine concentration in the West-Carpathian granites. Geologica
680 Carpathica, 53, 190–192.
681
682 Broska, I., Williams, C.T., Uher, P., Konečný, P., and Leichmann, J. (2004) The geochemistry
683 of phosphorus in different granite suites of the Western Carpathians, Slovakia: the role of
684 apatite and P-bearing feldspar. Chemical Geology, 205, 1–15.
685
686 Buda, G., and Pál-Molnár, E. (2012) Apatite as petrogenetic indicator of Variscan granitoids in
687 Tisza Mega-Unit (South Hungary). Carpathian Journal of Earth and Environmental Sciences, 7,
688 47–60.
689
690 Burchell, T.D. (1997) Radiation effects in graphite and carbon-based materials. MRS Bulletin,
691 22, 29-35.
692

693 Candela, P.A. (1989) Felsic magmas, volatiles, and metallogenesis. In J.A. Whiteny and A.J.
694 Naldrett, Eds., Ore deposits associated with magmas, Reviews in Economic Geology, 4, 223–
695 233.
696
697 Cao, M., Guangming, L., Kezhang, Q., Seitmuratova, E.Y., and Yongsheng, L. (2011) Major
698 and trace element characteristics of apatites in granitoids from Central Kazakhstan:
699 implications for petrogenesis and mineralization. Resource Geology, 62, 63–83.
700
701 Cao, M.-J., Zhou, Q.-F., Qin, K.-Z., Tang, D.-M., and Evans, N.J. (2013) The tetrad effect and
702 geochemistry of apatite from the Altay Koktokay No. 3 pegmatite, Xinjiang, China:
703 implications for pegmatite petrogenesis. Mineralogy and Petrology, 107, 985–1005.
704
705 Cherniak, D.J. (2005) Uranium and manganese diffusion in apatite. Chemical Geology, 219,
706 297–308.
707
708 Chu, M.F., Wang, K.L., Griffin, W.L., Chung, S.L., O'Reilly, S.Y., Pearson, N.J., and Iizuka,
709 Y. (2009) Apatite composition: tracing petrogenetic processes in Transhimalayan granitoids.
710 Journal of Petrology, 50, 1829–1855.
711
712 Cicconi, M. R., Giuli, G., Paris, E., Ertel-Ingrisch, W., Ulmer, P., and Dingwell, D.B. (2012)
713 Europium oxidation state and local structure in silicate glasses. American Mineralogist, 97,
714 918–929.
715

716 Comodi, P., Liu, Y., and Frezzotti, M.L. (2001) Structural and vibrational behaviour of
717 fluorapatite with pressure. Part II: in situ micro-Raman spectroscopic investigation. Physics
718 and Chemistry of Minerals, 28, 225–231.
719
720 Dawson, J.B. (1962) The geology of Oldoinyo Lengai. Bulletin Volcanologique, 24, 349–387.
721
722 De Toledo, M.C.M., Lenharo, S.L.R., Ferrari, V.C., Fontan, F., De Parseval, P., and Leroy, G.
723 (2004) The compositional evolution of apatite in the weathering profile of the Catãlao I
724 alkaline-carbonatitic complex, Brazil. The Canadian Mineralogist, 42, 1139–1158.
725
726 Dias, G., Leterrier, J., Mendes, A., Simoes, P.P., and Bertrand, J.M. (1998) U–Pb zircon and
727 monazite geochronology of syn to post-tectonic Hercynian granitoids from the Central Iberian
728 Zone (Northern Portugal). Lithos, 45, 349–369.
729
730 Dingwell, D.B., Knoche, R., and Webb, S.L. (1993) The effect of P_2O_5 on the viscosity of
731 haplogranitic liquids. European Journal of Mineralogy, 5, 133–140.
732
733 Doroshkevich, A.G., Wall, F., and Ripp, G.S. (2007) Magmatic graphite in dolomite
734 carbonatite at Pogranichnoe Nort Transbaikalia, Russia. Contributions to Mineralogy and
735 Petrology, 153, 339–353.
736
737 Duke, E.F., and Rumble, D. (1986) Textural and isotopic variations in graphite from plutonic
738 rocks, South Central New Hampshire. Contributions to Mineralogy and Petrology, 93, 409–
739 419.

740 Egerton, R.F. (1996) Electron Energy Loss Spectroscopy in the Electron Microscope (2nd ed.),
741 485 p. Plenum Press, New York

742 Elliot, J.C. (1994) Structure and chemistry of the apatites and other calcium orthophosphates.
743 Studies in Inorganic Chemistry 18, 389 p. Elsevier, Amsterdam.
744
745 Fleet, M.E., Liu, X., and Pan, Y. (2000) Rare-earth elements in chlorapatite [$Ca_{10}(PO_4)_6Cl_2$]:
746 Uptake, site preference, and degradation of monoclinic structure. American Mineralogist, 85,
747 1437–1446.
748
749 Fleet, M.E., and Pan, Y. (1995) Site preference of rare earth elements in fluorapatite. American
750 Mineralogist, 80, 329–335.
751
752 Freund, F. (1986) Solute carbon and carbon segregation in magnesium oxide single crystals – a
753 secondary ion mass spectrometry study. Physical and Chemistry of Minerals, 13, 262–276.
754
755 Frezzotti, M.L., Di Vincenzo, G., Ghezzo, C., and Burke, E.A. (1994) Evidence of magmatic
756 CO_2-rich fluids in peraluminous graphite-bearing leucogranites from Deep Freeze range
757 (northern Vivtoria Land, Antarctica). Contributions to Mineralogy and Petrology, 117, 111–
758 123.
759
760 García de Madinabeitia, S., Roda-Robles, E., Pesquera, A., Sánchez, M.E., and Gil Ibarguchi,
761 J.I. (2013) Characterization of complex Fe-Mn phosphates by LA-ICP-MS methods.
762 Mineralogical Magazine, 77, 1142.

763

764 Gellantly, D.C. (1966) Graphite in natural and experimental carbonate systems. Mineralogical
765 Magazine, 35, 936–970.

766

767 Göd, R. (1989) The spodumene deposit at “Weinebene”, Koralpe, Austria. Mineralium
768 Deposita, 24, 270–278.

769

770 Gottesmann, B., and Wirth, R. (1997) Pyrrhotite inclusions in dark pigmented apatite from
771 granitic rocks. European Journal of Mineralogy, 9, 491–500.

772

773 Hannah, J.L., and Stein, H.J. (1990) Magmatic and hydrothermal processes in ore-bearing
774 systems. In H.J. Stein and J.L. Hannah, Eds., Ore-bearing granite systems: petrogenesis and
775 mineralizing processes, 246, p. 1-10. The Geological Society, Special Paper, Boulder,
776 Colorado.

777

778 Harlov, D.E. (2015) Apatite: A fingerprint for metasomatic processes. Elements, 11, 171–176.

779

780 Harlov, D.E., Andersson, U.B., Förster, H.-J., Nyströmc, J.O., Dulski, P., and Broman, C.
781 (2002) Apatite–monazite relations in the Kiirunavaara magnetite–apatite ore, northern Sweden.
782 Chemical Geology, 191, 47–72.

783

784 Harlov, D., Renzulli, A., and Ridolfi, F. (2006) Iron-bearing chlor-fluorapatites in crustal
785 xenoliths from the Stromboli volcano (Aeolian Islands, Southern Italy): An indicator of fluid
786 processes during contact metamorphism. European Journal of Mineralogy, 18, 233–241.

Harrison, T.M., and Watson, E.B. (1984) The behavior of apatite during crustal anatexis: Equilibrium and kinetic considerations. Geochimica et Cosmochimica Acta, 48, 1467–1477.

Henderson, C.E. (2011) Protocols and pitfalls of electron microprobe analysis of apatite, 68 p. Master thesis, University of Michigan, Michigan, U.S.A.

Holzt, F., Dingwell, D.B., and Behrens, H. (1993) Effects of F, B_20_3 and P_2O_5 on the solubility of water in haplogranite melts compared to natural silicate melts. Contributions to Mineralogy and Petrology, 113, 492–501.

Hort, M. (1998) Abrupt change in magma liquidus temperature because of volatile loss or magma mixing: Effects on nucleation, crystal growth and thermal history of the magma. Journal of Petrology, 39, 1063–1076.

Hoshino, M., Kimata, M., Shimizu, M., and Nishida, N. (2007) Minor-element systematics of fluorapatite and zircon inclusions in allanite-(Ce) from three orogenic felsic rocks: implications for the origin of their host magmas. The Canadian Mineralogist, 45, 1337–1353.

Hoskin, P.W.O., Kinny, P.D., Wyborn, D., and Chappel, B.W. (2000) Identifying accessory minerals saturations during differentiation in granitoid magmas: and integrated approach. Journal of Petrology, 41, 1365–1396.

Hughes, J.M., Cameron, M., and Crowley, K.D. (1991) Ordering of divalent cations in the apatite structure: Crystal structure refinements of natural Mn- and Sr-bearing apatite. American Mineralogist, 76, 1857–1862.

Humphreys, M.C.S., Brooker, R.A., Fraser, D.G., Burgisser, A., Mangan, M.T., and McCammon, C. (2015). Coupled interactions between volatile activity and Fe oxidation state during arc crustal processes. Journal of Petrology, 56, 795–814.

Jackson, S.E., Pearson, N.J., Griffin, W.L., and Belousova, E.A. (2004) The application of laser ablation-inductively coupled plasma-mass spectrometry to in situ U-Pb zircon geochronology. Chemical Geology, 211, 47–69.

Jahnke, R.A. (1984) The synthesis and solubility of carbonate fluorapatite. American Journal of Science, 284, 58–78.

Jaszczak, J.A., and Trinchillo, D. (2013) Miracle at Merelani : A remarkable occurrence of graphite, diposide, and associated minerals from the Karo Mine, Block D, Merelani Hills, Arusha Region, Tanzania. Rocks & Minerals, 88, 154–165.

Kanaris-Sotiriou, R. (1997) Graphite-bearing peraluminous dacites from Erlend volcanic complex, Faeroe-Shetland Basin. North atlantic. Mineralogical Magazine, 61, 175–184.

Ketcham, R.A. (2015) Technical Note: Calculation of stoichiometry from EMP data for apatite and other phases with mixing on monovalent anion sites. American Mineralogist, 100, 1620–1623.

Kuehner, S.M., and Joswiak, D.J. (1996) Naturally occurring ferric ion sanidine from the Leucite Hills lamproite. American Mineralogist, 81, 229–237.

Kvasnitsa, V. N., Yatsenko, V. G., and Jaszczak, J. A. (1999) Disclinations in unusual graphite crystals from anorthosites of Ukraine. The Canadian Mineralogist, 35, 951–960.

London, D., Morgan, G.B. VI, Babb, H.A., and Loomis, J.L. (1993) Behaviour and effect of phosphorus in the system Na_2O–K_2O–Al_2O_3– SiO_2–P_2O_5–H_2O at 200 MPa (H_2O). Contributions to Mineralogy and Petrology,113, 50–465.

Long, J.M., Rakovan, J., Jaszczak, J.A., Sommer, A.J., and Anczkiewicz, R. (2013) Fluorapatite from a remarkable occurrence of graphite and associated minerals. Rocks & Minerals, 88, 179–183.

Luo, Y., Hughes, J.M., Rakovan, J., and Pan, Y. (2009) Site preference of U and Th in Cl, F, and Sr apatites. American Mineralogist, 94, 345–351.

Luque, F.J., Crespo-Feo, E., Barrenechea, J.F., and Ortega, L. (2012) Carbon isotopes of graphite: implications on fluid history. Geoscience Frontiers, 3, 197–207.

856 Luque, F.J., Pastyeris, J.D., Wopenka, B., Rodas, M., and Barrenechea, J.F. (1998) Natural
857 fluid-deposited graphite: mineralogical characteristics and mechanisms of formations.
858 American Journal of Sciences, 298, 471–498.
859
860 Mao, M., Rukhlov, A.S., Rowins, S.M., Spence, J., and Coogan, L.A. (2016) Apatite trace
861 element composition: a robust new tool for mineral exploration. Economic Geology 111,
862 1187–1222.
863
864 Macdonald, R., Bagiński, B., Belkin, H.E., Dzierżanowski, P., and Jeżak, L. (2008) REE
865 partitioning between apatite and melt in a peralkaline volcanic suite, Kenya Rift Valley.
866 Mineralogical Magazine, 72, 1147–1161.
867
868 Marks, M.A.W., Wenzel, T., Whitehouse, M.J., Loose, M., Zack, T., Barth, M., Worgard, L.,
869 Krasz, V., Eby, G.N., Stosnach, H., and Markl, G. (2012) The volatile inventory (F, Cl, Br, S,
870 C) of magmatic apatite: An integrated analytical approach. Chemical Geology, 291, 241–255.
871
872 Martín-Méndez, I., Boixereu, E., and Villaseca, C. (2016) Mineralogical and isotopic
873 characterization of graphite deposits from the Anatecti Complex of Toledo, central Spain.
874 Mineralium Deposita, 51, 575–590.
875
876 McClellan, G. H., and Lehr, J. R. (1969) Crystal chemical investigations of natural apatites.
877 American Mineralogist, 54, 1379–1391.
878

879 Merino, E. (2014) Geochemistry, U-Pb geochronology and Hf-isotope zircon composition of
880 Variscan granitoids from the Montes de Toledo batholith, 285 p. Ph.D. thesis, Universidad
881 Complutense de Madrid, Spain.
882
883 Merino, E., Villaseca, C., Orejana, D., and Jeffries, T. (2013) Gahnite, chrysoberyl and beryl
884 co-occurrence as accessory minerals in a highly fractionated evolved peraluminous pluton: the
885 Belvís de Monroy leucogranite (Cáceres, Spain). Lithos, 179, 137–156.
886
887 Merino Martínez, E., Villaseca, C., Orejana, D., Pérez-Soba, C., Belousova, E., and Andersen,
888 T. (2014) Tracing magma sources of three different S-type peraluminous granitoid series by in
889 situ U-Pb geochronology and Hf-isotope zircon composition: the Variscan Montes de Toledo
890 batholith (central Spain)**.** Lithos, 200–201, 273–298.
891
892 Miles, A.J., Graham, C.M., Hawkesworth, C.J., Gillespie, M.R., Hinton, R.W., and EIMF
893 (2013) Evidence for distinct stages of magma history recorded by the compositions of
894 accessory apatite and zircon. Contributions to Mineralogy and Petrology, 166, 1–19.
895
896 Miles, A.J., Graham, C.M., Hawkesworth, C.J., Gillespie, M.R., and Hinton, R.W. (2014) Mn
897 in apatite: A new redox proxy for silicic magmas?. Geochimica and Cosmochimica Acta, 132,
898 101–119.
899
900 Montanini, A., Tribuzio, R., and Bersani, D. (2010) Insights into the origin of mantle graphite
901 and sulphides in garnet pyroxenites from the External Liguride peridotites (Northern Apennine,
902 Italy). In M. Coltorti, H. Downes, M. Gregoire, and S.Y. O'Reilly, Eds., Petrological evolution

903 of the European lithospheric mantle, 337, p. 87–105. Geological Society, London, Special
904 Publications.
905
906 Murali, A.V., Parthasarathy, R., Mahadevan, T.M., and Sankar Das, M. (1983) Trace element
907 characteristics, REE patterns and partition coefficients of zircons from different geological
908 environments—A case study on Indian zircons. Geochimica et Cosmochimica Acta, 47, 2047–
909 2052.
910
911 Nasdala, L., Kronz, A., Wirth, R., Váczi, T., Pérez-Soba, C., Willner, A., and Kennedy, A.K.
912 (2009) The phenomenon of deficient electron microprobe totals in radiation-damaged and
913 altered zircon. Geochimica et Cosmochimica Acta, 73, 1637–1650.
914
915 Orejana, D., Merino, E., Villaseca, C., Pérez-Soba, C., and Cuesta, A. (2012) Electron
916 microprobe monazite geochronology of granitic intrusions from the Montes de Toledo
917 batholith (central Spain). Geological Journal, 47, 41–58.
918
919 Pan, Y., and Fleet, M.E. (2002) Compositions of the apatite-group minerals: substitution
920 mechanisms and controlling factors. In M.J. Kohn, J. Rakovan, and J.M. Hughes, Eds.,
921 Phosphates, 48, p. 13-49. Reviews in Mineralogy and Geochemistry, Mineralogical Society of
922 America, Chantilly, Virginia.
923
924 Pan, L.-C., Hu, R.Z., Wang, X.S., Bi, X.-W., Zhu, J.J., and Li, C. (2016) Apatite trace element
925 and halogen compositions as petrogenetic-metallogenic indicators: Examples from four granite
926 plutons in the Sanjiang region, SW China. Lithos, 254–255, 118–130.

Patel, A.R., and Deshapande, S.V. (1970) Whiskers growth in natural graphite. Carbon, 8, 242.

Pasero, M., Kampf, A.R., Ferraris, C., Pekov, I.V., Rakovan, J., and White, T.J. (2010) Nomenclature of the apatite supergroup minerals. European Journal of Mineralogy, 22, 163–179.

Peck, W.L., and Tumpane, K.P. (2007) Low carbon isotope ratios in apatite: An unreliable biomarker in igneous and metamorphic rocks. Chemical Geology, 245, 305–314.

Penn, R. L. (2004) Kinetics of oriented aggregation. The Journal of Physical Chemistry B, 108, 12707–12712.

Peretyazhko, I.S., Zagorsky, V.Y., Tsareva, E.A., and Sapozhnikov, A.N. (2007) Immiscibility of calcium fluoride and aluminosilicate melts in ongonite from the Ary-Bulak intrusion, Eastern Transbaikal Region. Doklady Earth Sciences, 413, 315–320.

Pérez-Soba, C., Villaseca, C., Orejana, D., and Jeffries, T. (2014) Uranium-rich accessory minerals in the peraluminous and perphosphorous granites of the Belvís de Monroy pluton (Iberian Variscan Belt). Contributions to Mineralogy and Petrology, 167, 1–25.

Piccoli, P.M., and Candela, P.A. (1994) Apatite in felsic rocks; a model for the estimation of initial halogen concentrations in the Bishop Tuff (Long Valley) and Tuolumne Intrusive Suite (Sierra Nevada Batholith) magmas. American Journal of Science, 294, 92–135.

Piccoli, P.M., and Candela, P.A. (2002) Apatite in igneous systems. In M.J. Kohn, J. Rakovan, and J.M. Hughes, Eds., Phosphates, 48, p. 255–292. Reviews in Mineralogy and Geochemistry, Mineralogical Society of America, Chantilly, Virginia.

Procházka,V., and Matějka, D. (2006) Rock-forming accessory minerals in the granites of the Melechov Massif (Moldanubian Batholith, Bohemian Massif). Acta Universitatis Carolinae, Geologica, 1-4, 71–79.

Prowatke, S., and Klemme, S. (2006) Trace element partitioning between apatite and silicate melts. Geochimica et Cosmochimica Acta, 70, 4513–4527.

Pyle, J.M., Spear, F., and Wark, D. (2002) Electron microprobe analysis of REE in apatite, monazite and xenotime: protocols and pitfalls. Reviews in Mineralogy and Geochemistry, 48, 337–362.

Raimbault, L., and Burnol, L. (1998) The Richemont rhyolite dyke, Massif Central, France: a subvolcanic equivalent of rare-earth granites. The Canadian Mineralogist, 36, 265–282.

Regnier, P., Lasaga, A.C., Berner, R.A., Han, O.H., and Zilm, K.W. (1994) Mechanism of CO_3^{2-} substitution in carbonate-fluorapatite: Evidence from FTIR spectroscopy, ^{13}C NMR, and quantum mechanical calculations. American Mineralogist, 79, 809–818.

Roda-Robles, E., Galliski, M.A., Roquet, M.B., Hatert, F., and De Parseval, P. (2012) Phosphate nodules containing two distinct assemblages in the Cema granitic pegmatite, San Luis province, Argentina: paragenesis, composition and significance in the pegmatite evolution. The Canadian Mineralogist, 50, 913–931.

Roeder, P.L., MacArthur, D., Ma, X.-P., Palmer, G.R., and Mariano, A.N. (1987) Cathodoluminescence and microprobe study of rare-earth elements in apatite. American Mineralogist, 72, 801–811.

Rosenberg, P.E. (1963) Subsolidus relations in the system $CaCO_3$-$FeCO_3$. American Journal of Science, 261, 683–690.

Rubatto, D. (2002) Zircon trace element geochemistry: partitioning with garnet and the link between U–Pb ages and metamorphism. Chemical Geology, 184, 123–138.

Rutherford, M.J., Hess, P.C., Daniel, G.H. (1974) Experimental liquid line of descent and liquid immiscibility for basalt 70017. Proceedings of the 5th Lunar Science Conference, 1, 569–583.

995 Seifert, W., Thomas, R., Rhede, D., and Förster, H.-J. (2010) Origin of coexisting wüstite, Mg–
996 Fe and REE phosphate minerals in graphite-bearing fluorapatite from the Rumburk granite.
997 European Journal of Mineralogy, 22, 495–507.
998
999 Sha, L.K., and Chappell, B.W. (1999) Apatite chemical composition, determined by electron
1000 microprobe and laser-ablation inductively coupled plasma mass spectrometry, as a probe into
1001 granite petrogenesis. Geochimica et Cosmochimica Acta, 63, 3861–3881.
1002
1003 Sirbescu, M.C., Leatherman, M.A., Student, J.J., and Beehr, A.R. (2009) Apatite textures and
1004 compositions as records of crystallization processes in the Animikie Red Ace pegmatite dike,
1005 Wisconsin, USA. The Canadian Mineralogist, 47, 725–743.
1006
1007 Sorbier, L., Rosenberg, E., and Merlet, C. (2004) Microanalysis of porous materials.
1008 Microscopy and Microanalysis, 10, 745–752.
1009
1010 Stormer, J.C., Jr., Pierson, M.L., and Tacker, R.C. (1993) Variation of F and Cl Xray intensity
1011 due to anisotropic diffusion in apatite during electron micorprobe analysis. American
1012 Mineralogist, 78, 641–648.
1013
1014 Strong, D.F. (1988). A review and model for granite-related mineral deposits. In R.P. Taylor,
1015 and D.F. Strong, Eds., Recent advances in the geology of granite-related mineral deposits, 39,
1016 p. 424–445. The Canadian Institute of Mining and Metallurgy Special Paper.
1017

Thomas, R., and Davidson, P. (2007) The formation of granitic pegmatites from the viewpoint of melt and fluid inclusions and new experimental work. Proceedings of the International Symposium Granitic Pegmatites: The State of the Art, Porto, Portugal.

Thomas, R., and Davidson, P. (2013) The missing link between granites and granitic pegmatites. Journal of Geoscience, 58, 183–200.

van Achterbergh, E., Ryan, C.G., Jackson, S.E., and Griffin, W. (2001) Data reduction software for LA–ICP–MS. In P. Sylvester, Ed., Laser Ablation ICPMS in the Earth Sciences, 29, p. 239–243. Mineralogical Association of Canada, Short Course Series.

Veksler, I.V., Dorfman, A.M., Dulski, P., Kamenetsky, V.S., Danyushevsky, L.V., Jeffries, T., and Dingwell, D.B. (2012) Partitioning of elements between silicate melt and immiscible fluoride, chloride, carbonate, phosphate and sulfate melts, with implications to the origin of natrocarbonatite. Geochimica et Cosmochimica Acta, 79, 20–40.

Veksler, I.V., Thomas, R., and Schmidt, C. (2002) Experimental evidence of three coexisting immiscible fluids in synthetic granite pegmatite. American Mineralogist, 87, 775–779.

Villaseca, C., Barbero, L., and Rogers, G. (1998) Crustal origin of Hercynian peraluminous granitic batholiths of central Spain: petrological, geochemical and isotopic (Sr, Nd) constraints. Lithos, 43, 55–79.

Villaseca, C., Pérez-Soba, C., Merino, E., Orejana, D., López-García, J.A., and Billstrom, K. (2008) Contrasting crustal sources for peraluminous granites of the segmented Montes de Toledo Batholith (Iberian Variscan Belt). Journal of Geoscience, 53, 263–280.

Villaseca, C., Merino, E., Oyarzun, R., Orejana, D., Pérez-Soba, C., and Chicharro, E. (2014) Contrasting chemical and isotopic signatures from Neoproterozoic metasedimentary rocks in the Central-Iberian Zone of pre-Variscan Europe (Spain): Implications for terrane analysis and Early Ordovician magmatic belts. Precambrian Research, 245, 131–145.

Webster, J.D., and Piccoli, P.M. (2015) Magmatic apatite: A powerful, yet deceptive, mineral. Elements, 11, 177–182.

Weiss, P.L., Friedman, I., and Gleason, J.P. (1981) The origin of epigenetic graphite: evidence from isotopes. Geochimica et Cosmochimica Acta, 45, 2325–2332.

Winchell, A.V. (1911) A theory for the origin of graphite as exemplified by the graphite deposit near Dillon, Montana. Economic Geology, 6, 218–230.

Wolf, M.B., and London, D. (1994) Apatite dissolution into peraluminous haplogranitic melts: An experimental study of solubilities and mechanisms. Geochimica et Cosmochimica Acta, 58, 4127–4145.

1063 Wolf, M.B., and London, D. (1995) Incongruent dissolution of REE- and Sr-rich apatite in
1064 peraluminous granitic liquids: differential apatite, monazite, and xenotime solubilities during
1065 anatexis. American Mineralogist, 80, 765–775.
1066
1067 Wopenka, B., and Pasteris, J.D. (2005) A mineralogical perspective on the apatite in bone.
1068 Materials Science and Engineering C, 25, 131–143.
1069
1070 Yi, H., Balan, E., Gervais, C., Segalen, L., Fayon, F., Roche, D., Person, A., Morin, G.,
1071 Guillaumet, M., Blanchard, M., Lazzeri, M., and Babonneau, F. (2013) A carbonate-fluoride
1072 defect model for carbonate-rich fluorapatite. American Mineralogist, 98, 1066–1069.
1073
1074 Zeck, H.P. (1992) Restite-melt and mafic-felsic magma mixing and mingling in an S-type
1075 dacite, Cerro del Hoyazo, southeastern Spain. Transactions of the Royal Society of Edinburgh,
1076 83, 139–144.
1077
1078 Zhang, S., Wang, L., and Yang, W. (1985) Use of REE analysis in apatite to distinguish
1079 petrological and mineralogical series of granitic rocks. Geochimica, 1, 45–57.
1080
1081 Zirner, A.L.K., Marks, M.A.W., Wenzel, T., Jacob, D.E., and Markl, G. (2015) Rare earth
1082 elements in apatite as a monitor of magmatic and metasomatic processes: The Ilímaussaq
1083 complex, South Greenland. Lithos, 228–229, 12–22.
1084

Figure captions

Figure 1. Photomicrograph showing textures of the type 1 (**a-b**), type 2 (**c-h**) and type 3 (**i-l**) apatite in the Belvís granites. SEM = Secondary electron images, BSE= Back scattered electron images. BSE images of euhedral and equant type 1 apatite (**a**) and subhedral and equant type 1 apatite (**b**); (**c**) anhedral dusty sections of apatite 2 under petrographic microscope (plane polarized light); (**d-e**) BSE image of large and dusty interlobate crystals of type 2 apatite, mainly interstitial to granite-rock forming minerals, with dark irregular areas (richer in graphite inclusions) and frequent intragranular cracks; (**f**) SEM-BSE image of inclusions of graphite crystals arranged in parallel (BSE dark) within type 2 apatite (BSE light), defining different areas according to inclusion-density; (**g**) SEM-BSE image of subhedral and equant type-2 apatite, plenty of graphite microinclusions randomly oriented, as it is possible to observe in detail from (**h**) image; (**i**) BSE image of an anhedral section of type 3 apatite, with the characteristic feathered aggregate texture, and partially replaced by childrenite- eosphorite-(chil-eos); (**j-l**) SEM-BSE images of different appearances of the feather texture in different crystals of type 3 apatite, irregular (**j**), oriented (**k**), or without preferential orientation (**l**).

Figure 2. Compositional variation for the three apatite types of the Belvís granites: (**a**) Plot of FeO and MnO variation, with 1:2 vector defining the main trend for type 1 and type 2, and vector 1:1 for type 3 apatite. (**b**) Plot of LREE and Sr abundance. (**c**) Plot of Zr and Hf abundance. (**d**) Plot of Th and U abundances for apatite from Belvís and compositional fields of apatite from different magmatic suites: I-type granite: Hoskin et al. (2000) (Boggy Plain pluton, Australia); Chu et al. (2009) (Transhimalayan granitoids); Cao et al. (2011) (Central Kazakhstan, Kazagistan), Pan et al. (2016) (Pulang and Xiuwacu plutons, Zhongdian terrane, China); S-type granite: Sha et al. (2009) (Lachlan Fold Belt, Australia), Chu et al. (2009)

(Transhimalayan granitoids); LCT pegmatite :Cao et al. (2013) (Altai Orogen, China); alkaline felsic rocks : Zirner et al. (2015) (Ilímaussaq complex, South Greenland). (**e**) Plot of Na and Cl abundances; the arrow remarks the broad positive correlation shown by type 3 apatite.. (**f**) Plot of analytical total (wt%) and CaO abundance.

Figure 3. REE contents of apatite types from the Belvís granites (**a**) Plot of Y+HREE and LREE contents. (**b**) Chondrite-normalized plot showing the REE patterns of type 2 grouped in a grey area for a better comparison with type 1. Owing to the extremely low REE content in type 3 apatite, values just above the detection limits have been used. (c) Plot of REE fractionation $(La/Yb)_N$ ratios against the Eu anomaly for type 1 and type 2 apatite.

Figure 4. Secondary electron images of cracked apatite surfaces illustrating shape and size of graphite inclusions in fluorapatite host. (**a-b**) Variably sized graphite inclusions (filaments), randomly orientated; (**c**) Graphite inclusions showing the typical cavity around them; (**d**) Detail of graphite inclusion composed by graphene stack.

Figure 5. Secondary electron images of graphite inclusions in fluorapatite, with X-ray EDS profiles (white line) crossing the graphite microinclusions for C, Ca, P and F. The profiles are performed along two graphite filaments with different crystal orientations.

Figure 6. Carbon isotope compositions of the Belvís granites and the nearby Navalmoral pluton according to the estimated emplacement temperatures. Carbon (biogenic, mantle and carbonates) compositional fields have been included (Martín-Méndez et al. 2016, and references therein). Biogenic carbon isotopic data from different sectors of the Central Iberian

Zone (at their estimated metamorphic conditions): pelitic wall-rocks from the Schist-Greywacke Complex (SGC), migmatitic metapelites from the Anatectic Complex of Toledo (ACT), and pelitic granulites from lower crustal xenoliths (LC) are taken from Table 2 and from Martín-Méndez et al. (2016).

Figure 7. Compositional variation of the three apatite types of the Belvís granites: (**a**) Plot of variation of the anionic site between Cl and F. (**b**) Plot of Ca and F contents, remarking the lack of correlation in type 1 and type 2 apatite. (**c**) Plot of Cl and Li contents. (**d**) Plot of (Y+REE) and Li contents. (**e**) Plot of Na and Li content. (**g**) Plot of Fe and Na.

Figure 8. REE compositional variation of the three apatite types of the Belvís granites: (**a**) Plot of Ce and Eu anomalies of the three apatite types and the variation trends for the oxygen fugacity according to data from the literature (Roeder et al. 1987; Sha and Chappel 1999; Broska et al. 2002; Cao et al. 2011);. (**b**) Plot of (Y + HREE) and LREE contents; type 3 apatite is outlined due to their projection close to the origin of coordinates. (**c**) Plot of $(La/Sm)_N$ vs. (Y + HREE) contents including the compositional track records of apatite if monazite and xenotime, respectively, decrease its crystallization rate ("decreasing influence"); type 3 apatite compositional field is outlined to stress the low REE values.

This is a preprint, the final version is subject to change, of the American Mineralogist (MSA)
Cite as Authors (Year) Title. American Mineralogist, in press.
(DOI will not work until issue is live.) DOI: http://dx.doi.org/10.2138/am-2017-5895

ELECTRONIC SUPPLEMENT

Figure captions

Figure 1. (**a**) Summarized geological map of the Central Iberian Zone (CIZ) displaying the two main batholithic areas referenced in this paper: the Spanish Central System (SCS) and the Montes de Toledo (MT). (**b**) Geological map of the Belvís pluton modified from Pérez-Soba et al. (2014). Sample location of granites with analyzed apatite included in Appendix[1] Table 1 (black asterisk: type 1 apatite; white asterisk: type 2 apatite; number sign: type 3 apatite).

Figure 2. Outcrop features of the wall-rock and the Belvís pluton granites: (**a)** and **(b**) Schist Greywacke Complex, a monotonous sequence of metapelites and metasamites variably affected by contact metamorphism. (**c**) Cordierite-bearing muscovite leucogranite (G1) exhibiting magmatic foliation and abundant cordierite-quartz nodules. (**d**) Muscovite-bearing biotite leucogranite medium grained (G3), with a well defined magmatic foliation (parallel to the pencil).

Figure 3. Photomicrographs (plane-polarized light) in samples from G3 Belvís granite showing textural features and its relationships with the main-rock forming minerals: (**a**) Thin section of a sample from the G3 granite from the Belvís pluton, with orange dots pointing the localization of type 2 apatite crystals. (**b**) Apatite type 2 crystals showing the typical dusty and anhedral appearance, with frequents microcraks. (**c**) Type 2 apatite, exceptionally clear, but including graphite isolated filaments, most of them showing radial disposition. (**d**) Cluster of three dusty and anhedral type 2 apatite crystals interlocked mainly with biotite and muscovite. (**e**) Type 2 apatite crystals interlocked with k feldspar, biotite, muscovite and quartz.

This is a preprint, the final version is subject to change, of the American Mineralogist (MSA)
Cite as Authors (Year) Title. American Mineralogist, in press.
(DOI will not work until issue is live.) DOI: http://dx.doi.org/10.2138/am-2017-5895

TABLE 1. General features of fluorapatite types in the Belvís granite units

	TYPE 1	TYPE 2	TYPE 3
Occurrence in the Belvís granite units G1 G2 G3 G4 more evolved ← less evolved	G1-G2-G3-G4	G2-G3-G4 (more abundant in the least fractionated granite)	G1 (the highest fractionated granite)
Apatite appearance	clear, greenish	dusty	feathery aggregate
Apatite shape	euhedral (equant) to anhedral	anhedral (interlobate) to euhedral	anhedral to subhedral
Apatite size	90% crystals: 20- 600 µm 10% crystals: 900–2000 µm	250 – 2000 µm	50 - 3000 µm
Framework position	hosted in feldspars, quartz and micas	interstitial	interstitial
Remarkable mineral association		graphite inclusions	occasional inclusions of childrenite-eosphorite
Main chemical features	MnO < 4.30 wt% FeO_t < 2.53 wt%		MnO < 4.17 wt% FeO_t < 5.09 wt% (mainly as Fe_2O_3)
	REE + Y = 2125 – 9150 ppm High U contents (156 - 460 ppm) Na_2O < 0.24 wt (except. one of 0.46 wt%)		Low Y, REE contents (bdl) Low U contents (< 75 ppm) Na_2O = 0.16 - 0.83 wt%
	LREE = 1231 - 2932 ppm Sr = 33-81 ppm Eu anomaly = 0.072 -0.794	LREE = 3163 - 4048 ppm Sr = 67-203 ppm Eu anomaly = 0.076 -0.233	High Sr contents (1596 – 2490 ppm) Significant Cl, Li, B, Be, Zn contents

Notes: Childrenite-eosphorite serie: $(Fe, Mn)^{2+}Al(PO_4)(OH)_2 \cdot H_2O$; bdl = below detection limits; FeO_t = Fe total expressed as FeO.

This is a preprint, the final version is subject to change, of the American Mineralogist (MSA)
Cite as Authors (Year) Title. American Mineralogist, in press.
(DOI will not work until issue is live.) DOI: http://dx.doi.org/10.2138/am-2017-5895

TABLE 2. Carbon isotope composition for metasedimentary wall-rocks and granites of the Montes de Toledo batholith

Lithology	Sample	weight (mgr)	$\delta^{13}C$ (‰)	**± 1σ**
Slates (SGC)	110194	1.4	-31.00	0.22
	111966	6.2	-32.49	0.30
Navalmoral de la Mata granites	106804	41.6	-29.24	0.53
	110183	41.9	-32.78	0.11
Belvís granites	106792 (G1)	40.2	-27.38	0.18
	106796 (G2)	42.5	-25.20	0.21
	111401 (G3)	41.2	-24.35	0.05

Note: SGC = Schist Greywacke Complex; G1, G2 and G3 are granite units of the Belvís pluton.

This is a preprint, the final version is subject to change, of the American Mineralogist (MSA)
Cite as Authors (Year) Title. American Mineralogist, in press.
(DOI will not work until issue is live.) DOI: http://dx.doi.org/10.2138/am-2017-5895

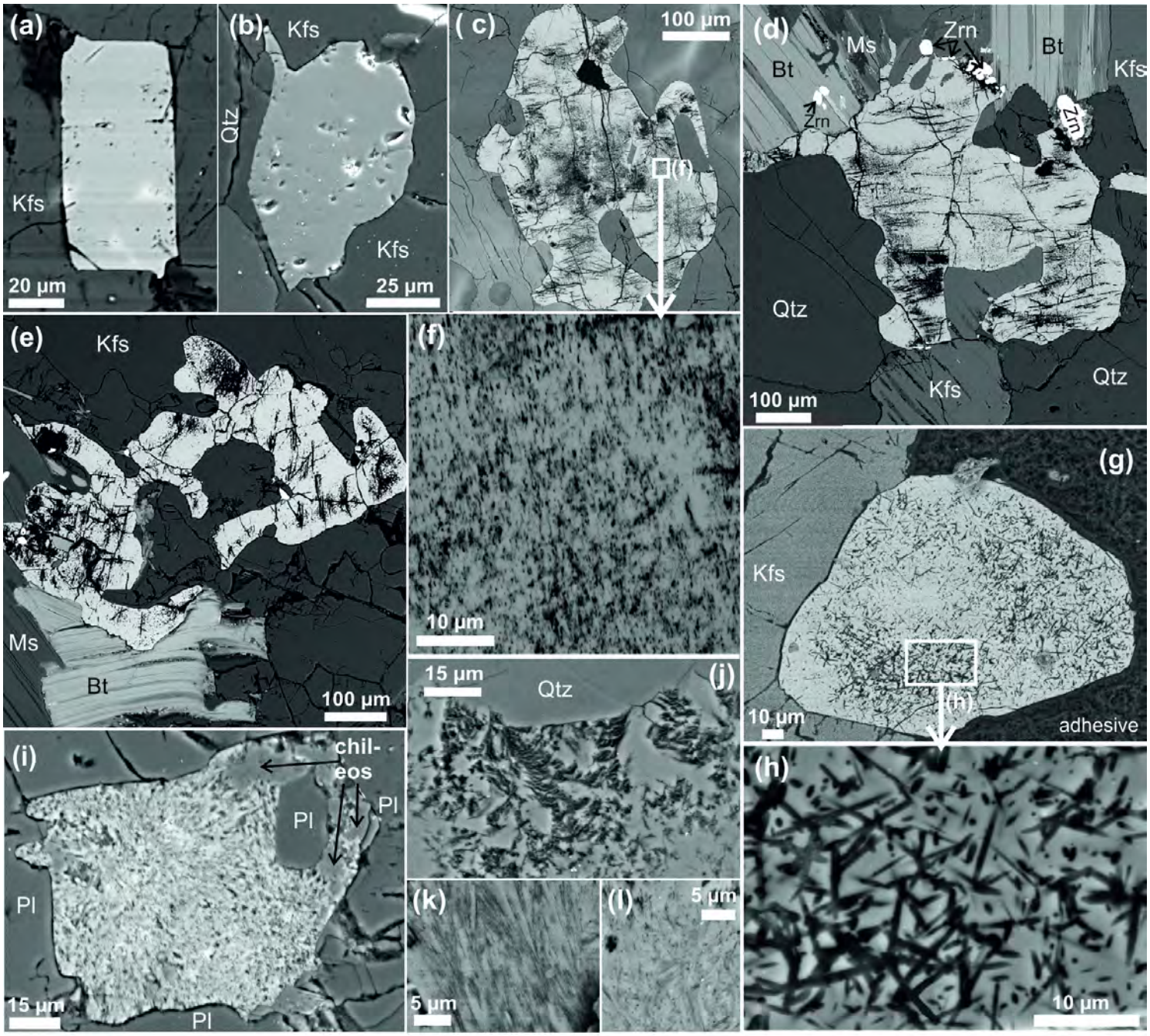

Figure 1

This is a preprint, the final version is subject to change, of the American Mineralogist (MSA)
Cite as Authors (Year) Title. American Mineralogist, in press.
(DOI will not work until issue is live.) DOI: http://dx.doi.org/10.2138/am-2017-5895

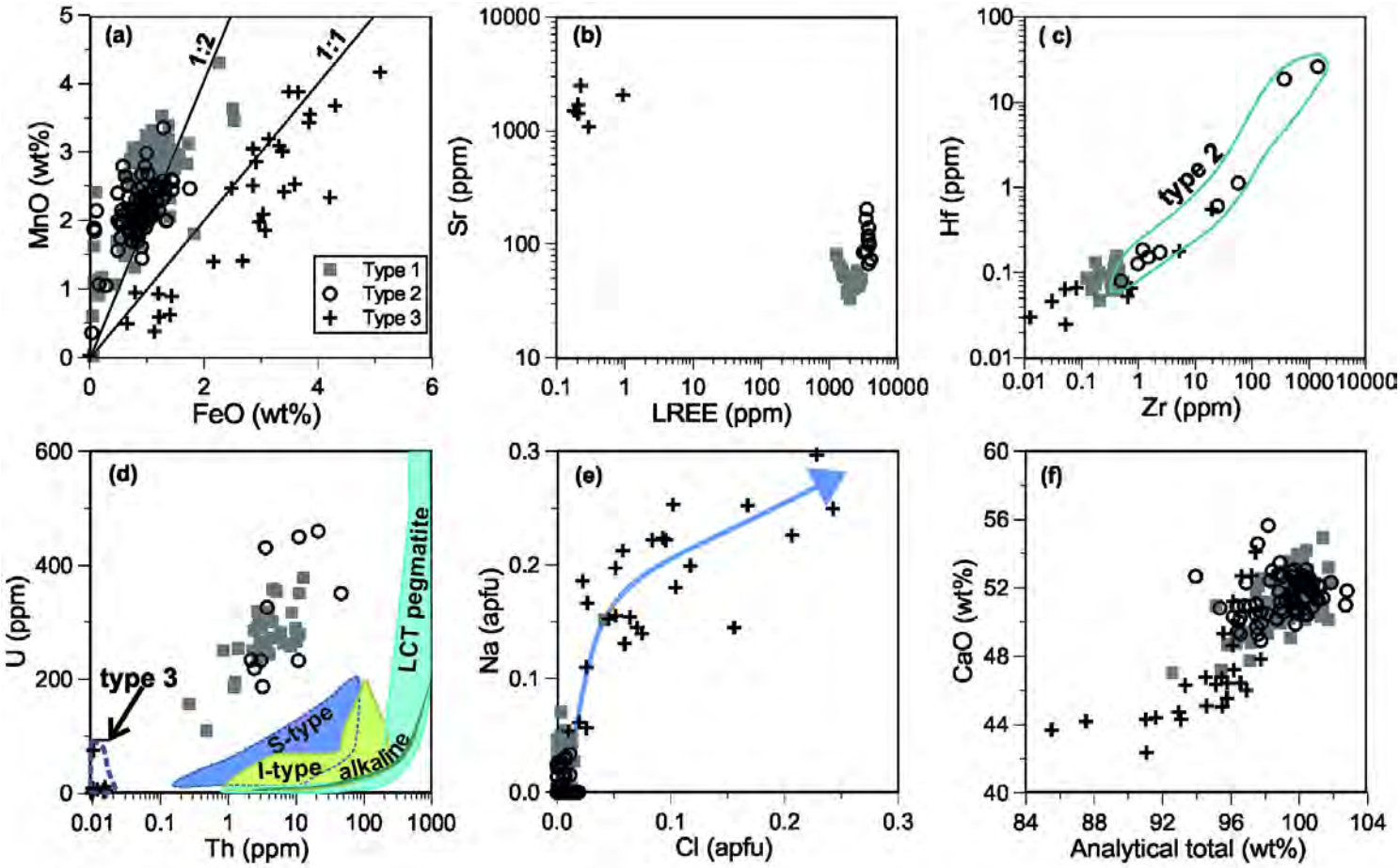

Figure 2

This is a preprint, the final version is subject to change, of the American Mineralogist (MSA)
Cite as Authors (Year) Title. American Mineralogist, in press.
(DOI will not work until issue is live.) DOI: http://dx.doi.org/10.2138/am-2017-5895

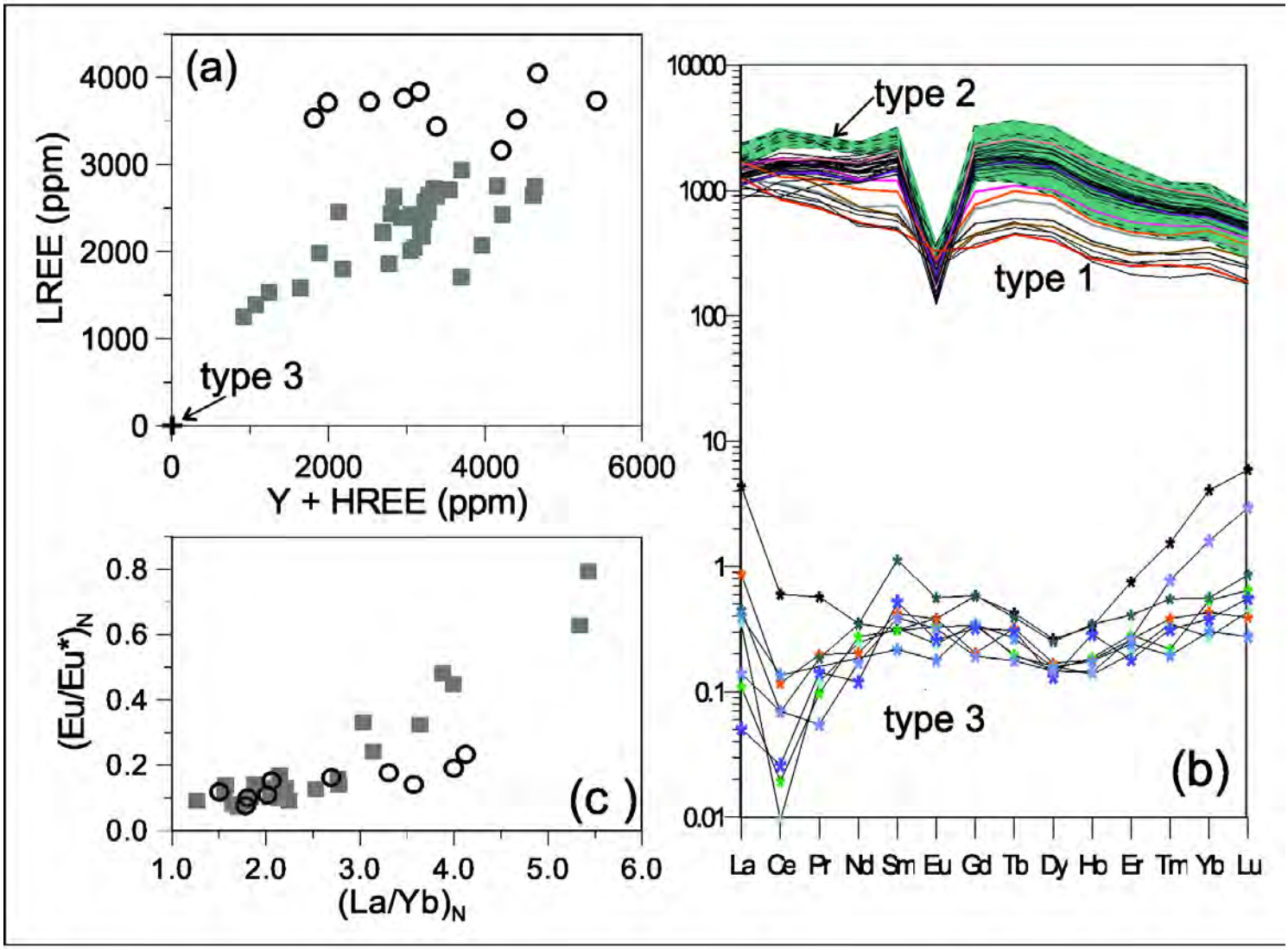

Figure 3

This is a preprint, the final version is subject to change, of the American Mineralogist (MSA)
Cite as Authors (Year) Title. American Mineralogist, in press.
(DOI will not work until issue is live.) DOI: http://dx.doi.org/10.2138/am-2017-5895

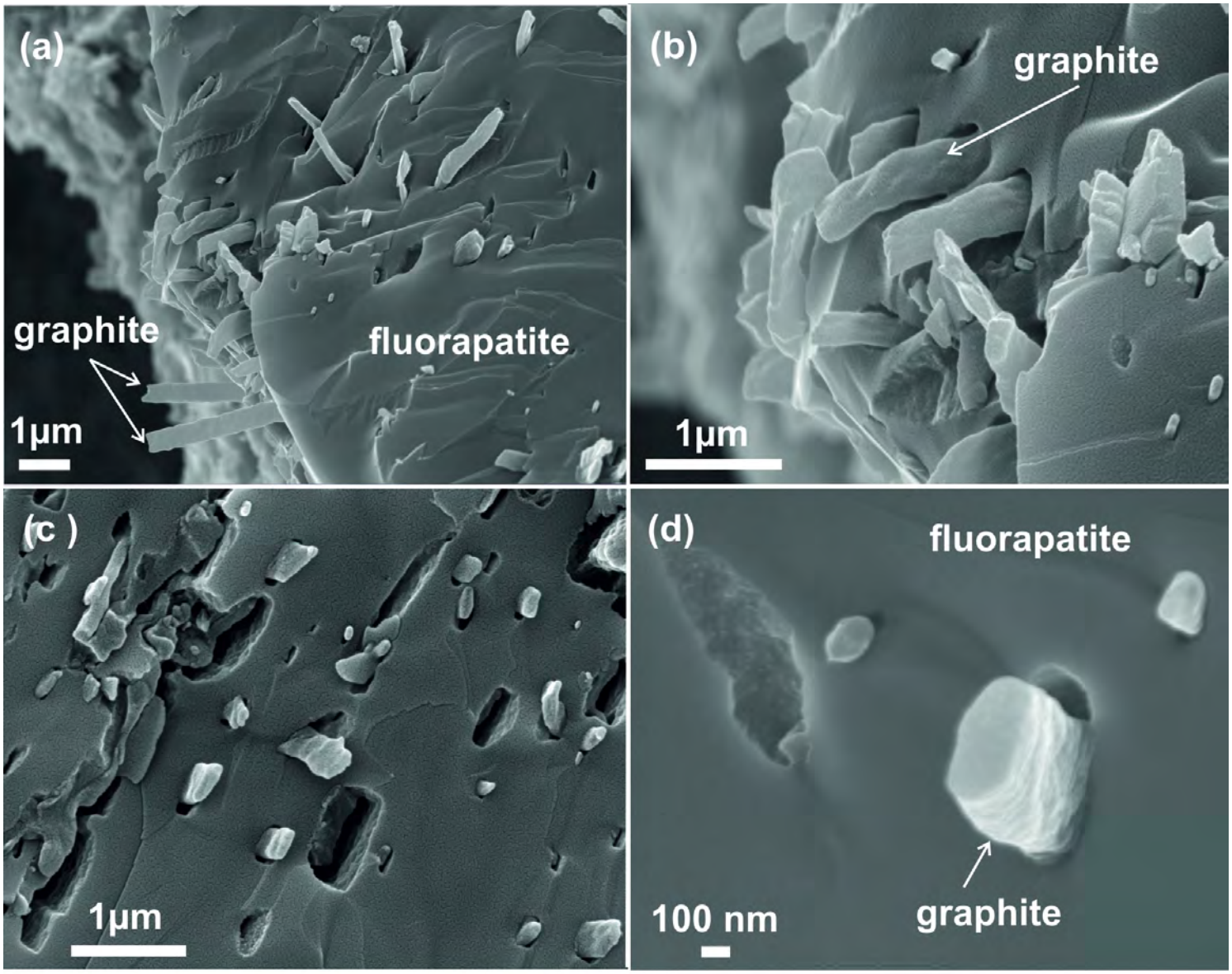

Figure 4

This is a preprint, the final version is subject to change, of the American Mineralogist (MSA)
Cite as Authors (Year) Title. American Mineralogist, in press.
(DOI will not work until issue is live.) DOI: http://dx.doi.org/10.2138/am-2017-5895

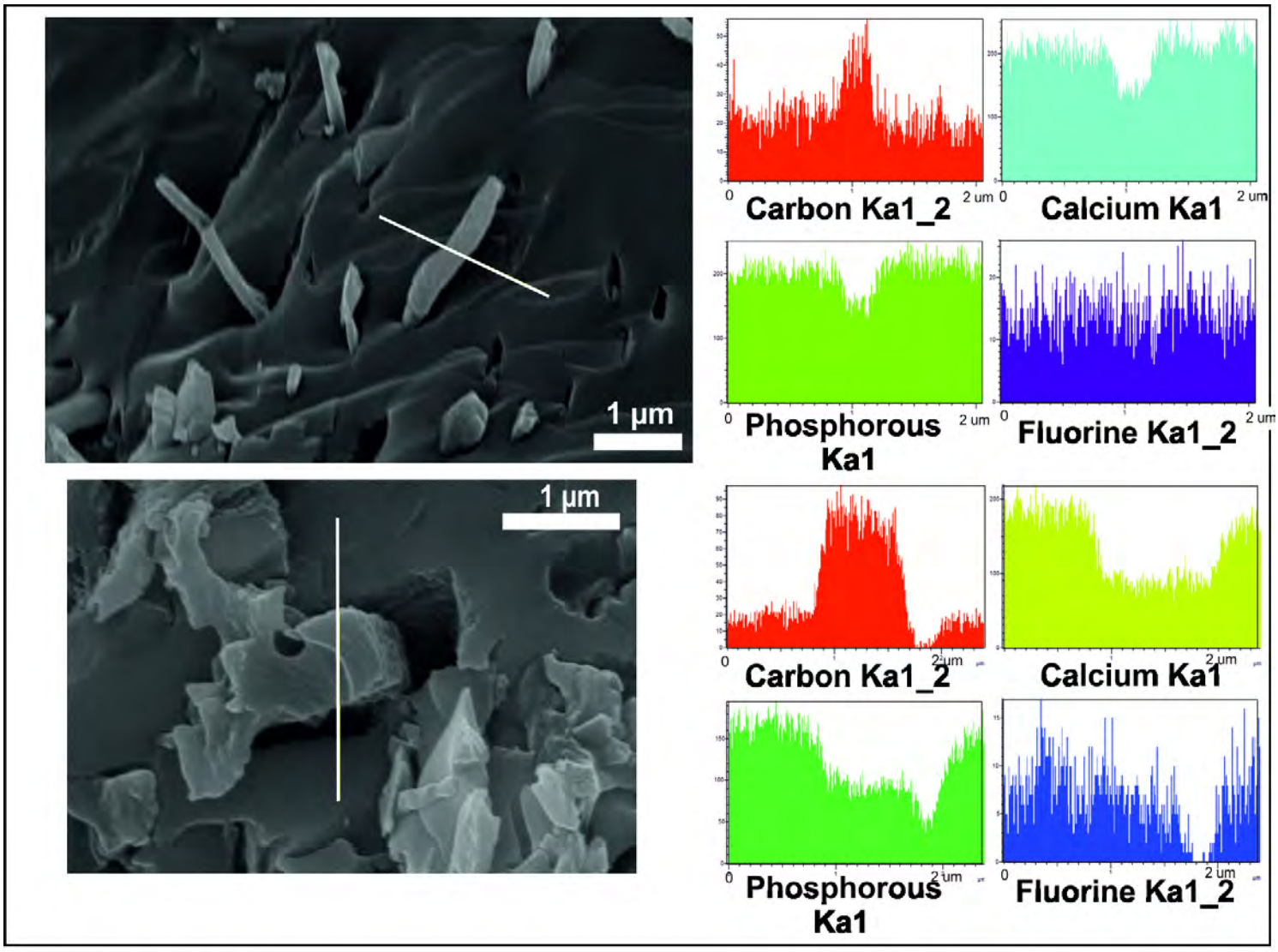

Figure 5

This is a preprint, the final version is subject to change, of the American Mineralogist (MSA)
Cite as Authors (Year) Title. American Mineralogist, in press.
(DOI will not work until issue is live.) DOI: http://dx.doi.org/10.2138/am-2017-5895

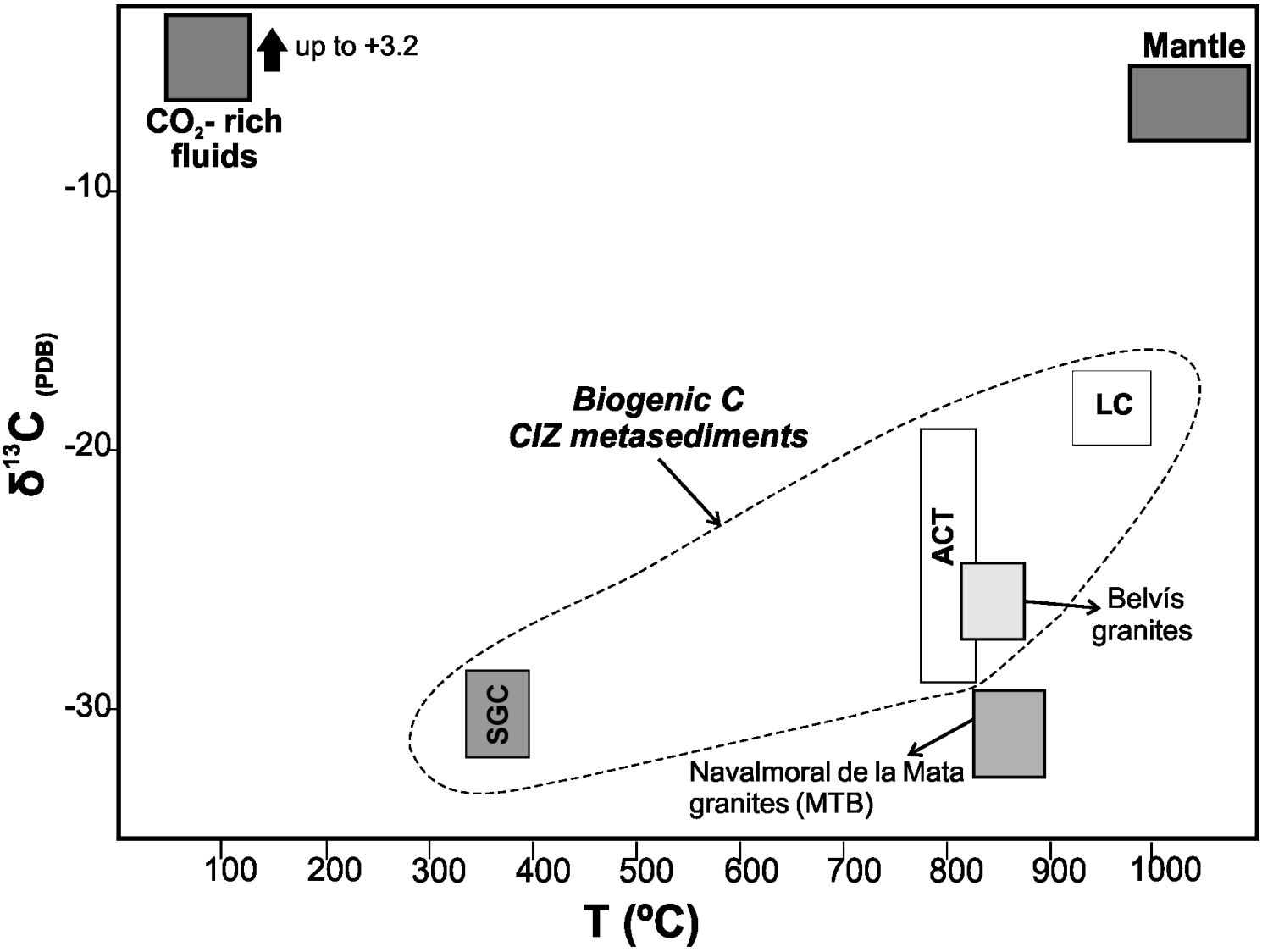

Figure 6

This is a preprint, the final version is subject to change, of the American Mineralogist (MSA)
Cite as Authors (Year) Title. American Mineralogist, in press.
(DOI will not work until issue is live.) DOI: http://dx.doi.org/10.2138/am-2017-5895

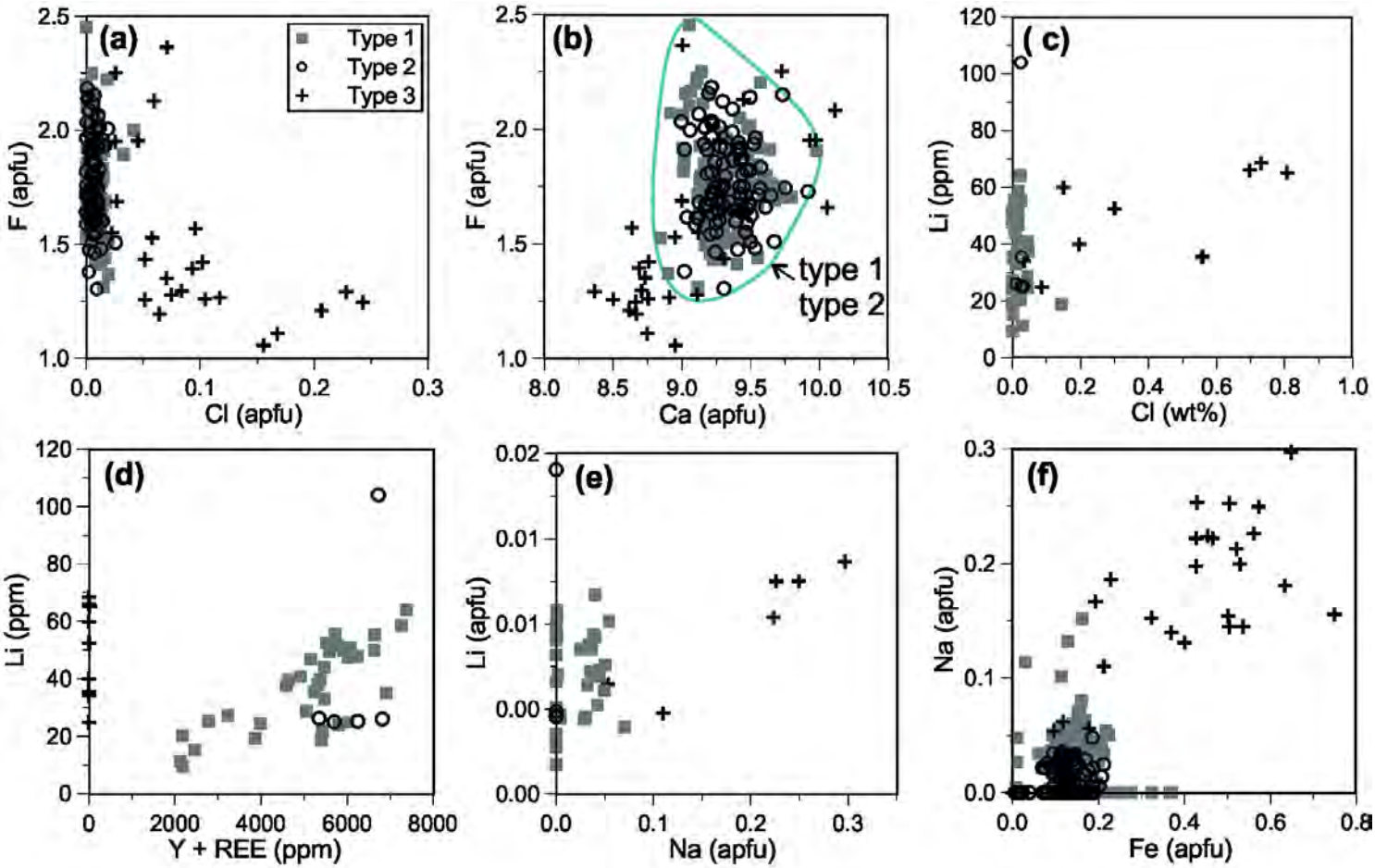

Figure 7

This is a preprint, the final version is subject to change, of the American Mineralogist (MSA)
Cite as Authors (Year) Title. American Mineralogist, in press.
(DOI will not work until issue is live.) DOI: http://dx.doi.org/10.2138/am-2017-5895

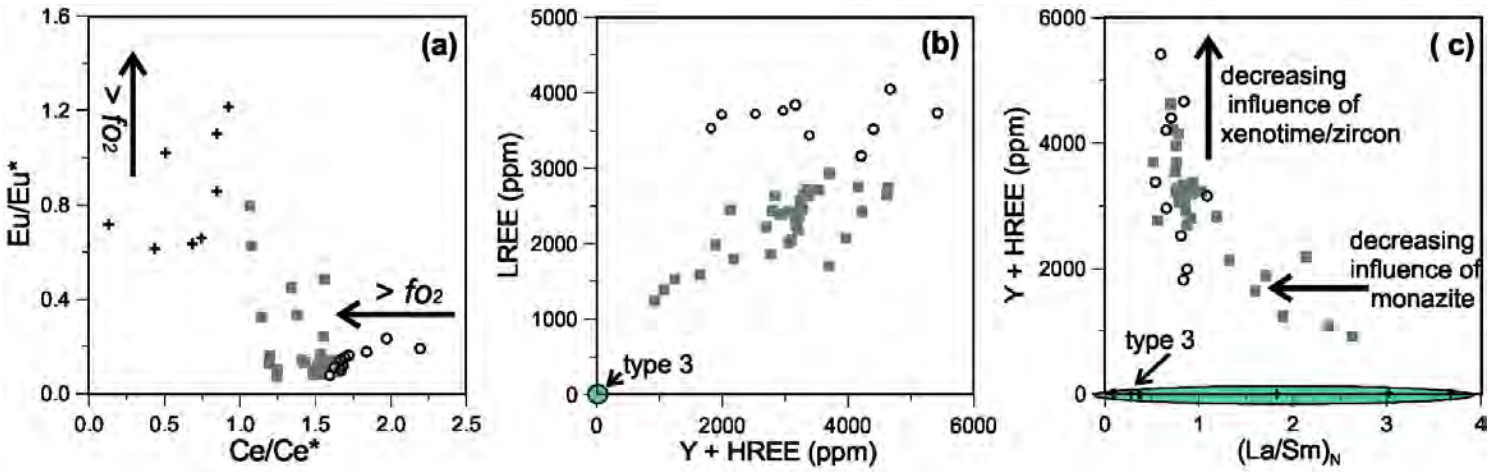

Figure 8